



# Impact of silver-doped alumina nanocomposite on water decontamination by remodeling of biogenic waste

Seham Alterary<sup>1</sup> · Musarat Amina<sup>2</sup> · Maha El-Tohamy<sup>1</sup>

Received: 20 January 2023 / Accepted: 23 May 2023 / Published online: 30 May 2023  
© The Author(s), under exclusive licence to Springer-Verlag GmbH Germany, part of Springer Nature 2023

## Abstract

The main cause of various fatal diseases in humans and animals is environmental pollution. Ag-doped alumina nanocomposite was prepared using coffee husk extract with a large BET surface area of  $126.58 \text{ m}^2 \text{ g}^{-1}$  and investigated for its antibacterial potential against both bacterial strains *Escherichia coli* and *Salmonella typhimurium*, and observed as an effective sorbent for removing the water pollution dye indigo carmine (IGC). The lowest concentration of the nanocomposite and the maximum contact time required to achieve complete inhibition of bacteria present in the contaminated water, as well as the capacity of sorption of IGC, were investigated. The results showed that the minimum inhibitory concentration of the Ag-doped alumina nanocomposite was  $12 \mu\text{g mL}^{-1}$  for both bacterial strains, with the highest inhibition occurring in *E. coli*. Moreover, the nanocomposite exhibited an experimental  $q_t$  of  $462.7 \text{ mg g}^{-1}$  from  $160 \text{ mg L}^{-1}$  IGC solution at  $50^\circ\text{C}$  and followed the Langmuir model. The thermodynamic results showed that the process was endothermic, spontaneous, and physisorptive. The nanocomposite was used to fully treat water samples contaminated with  $10 \text{ mg L}^{-1}$  concentrations of IGC. For six consecutive cycles, the reuse research showed an average efficiency of  $95.72 \pm 3.6\%$ . Consequently, the synthesized Ag-doped alumina nanocomposite is suitable for treatments of contaminated water.

**Keywords** Water decontamination · Nanomaterials · Silver-doped metal oxide · Nanocomposite · Antibacterial · Dye removal

## Introduction

Hygienic water is currently a widespread global issue. Safe drinking water is both a survival necessity and an ecological niche. Yet, negligence and mismanagement of water reservoirs have put the availability of fresh water at risk. Every year, millions of people die as a result of contaminated water

and waterborne diseases (Kumar et al. 2022). Waterborne infections are undeniably caused by microorganisms. Coliform germs are a good indicator of current fecal excretion. Waterborne microbial infections are one of the leading causes of death (Luo et al. 2022).

Inorganic elements and heavy metals, although not very harmful in small amounts, can act as toxic waste in water over time. Organic contaminants, on the other hand, enter water bodies in similar ways: intentional dumping, leaching, industrial disasters, and human activities (Astuti et al. 2023).

This type of polluted water, especially in areas with high water intake, can cause serious health problems and even death in humans and other living things. In addition, organic pollutants and toxic substances from industrial wastes cause an acute stalemate between environmental and health problems. Aquatic fauna and flora are affected by trace amounts of dyes, as they are carcinogenic by nature. In particular, cationic dyes are more toxic than anionic dyes due to their aromatic ring arrangement with delocalized electrons and their synthetic nature (Karthigadevi et al. 2021). Moreover,

Responsible Editor: Angeles Blanco

✉ Seham Alterary  
salterary@ksu.edu.sa

Musarat Amina  
mamina@ksu.edu.sa

Maha El-Tohamy  
moraby@ksu.edu.sa

<sup>1</sup> Department of Chemistry, College of Science, King Saud University, P.O. Box 22452, Riyadh 11495, Saudi Arabia

<sup>2</sup> Department of Pharmacognosy, Pharmacy College, King Saud University, P.O. Box 22452, Riyadh 11495, Saudi Arabia

the presence of these dyes reduces the productivity of agricultural land (Singh et al. 2021a).

Removing dye molecules from polluted water is now a top priority before it enters waterways. Considering the expected global demand for clean water, especially in Saudi Arabia, there is a strong push to develop low-cost, high-efficiency wastewater treatment systems and materials (Balabel and Alwetaishi 2021).

Various methods such as membrane separation, coagulation, photocatalysis, ion exchange, electrocoagulation, and adsorption are used to purify polluted water (Singh et al. 2021b; Sajjadifar 2017; Jabbar et al. 2022; Zhang et al. 2021; Al-Juboori et al. 2022; Shokri and Fard 2022; Rashid et al. 2021; Hiawi and Ali 2022). Among all available methods, adsorption is considered a cost-effective and easy-to-use approach for the purification of polluted water and can be applied from small residential units to large industrial facilities (Koh et al. 2022). A variety of conventional adsorbents, from activated carbon to inorganic wastes, have been investigated for wastewater treatment by a number of researchers worldwide (Lotfy and Roubik 2021; Lewoyehu 2021; Raza et al. 2022). However, most conventional adsorbents have non-uniform pore structure and low specific surface area, resulting in low adsorption capacity (Dou et al. 2022).

Recently, the use of nanomaterials such as nanoadsorbents, polymeric nanocomposites, and metal-doped nanomaterials has gained tremendous attention due to their unique properties that have a large number of active sites (Adeleye et al. 2016). A number of metal oxides such as zinc oxide, zirconium oxide, titanium oxide, binary metal oxides, and a combination of different metal oxides have been used to purify contaminated water and were found to be very effective compared to conventional adsorbents (Wang et al. 2020). Among various nanomaterials, alumina-based nanostructures are widely used due to their high pollution efficiency, cost efficiency, low energy intensity, and low environmental impact (Xie et al. 2015). Aluminum-based nanostructures are composed of metallic aluminum and alumina. Alumina nanoparticles are widely used for various applications, including biomedicine, drug delivery vehicles, ophthalmology, electronic devices, and as catalysts in various industrial processes (Roy 2021; Hassanpour et al. 2018; Wang et al. 2016; Yang et al. 2018; Atrak et al. 2018).

Metallic aluminum nanoparticles are very reactive and cannot be used in water treatment processes. However, the use of nano- $\text{Al}_2\text{O}_3$ /hydrolyzed  $\text{Al}_2\text{O}_3$  as adsorbents to regulate harmful ions in wastewater is very common (Ravindhranath and Ramamoorthy 2017). The  $\text{Al}_2\text{O}_3$  nanoparticles have shown versatile adsorption properties in decontamination of water/wastewater due to their large surface area, availability of surface groups to bind the pollutants and high surface energy (Sharma et al. 2021). The United Nations Environment Program (UNEP) has also

recommended alumina-based adsorption as one of the best waste treatment technologies currently available (Prabha-kar and Samadder 2018).

The literature survey described the synthesis of silver-doped alumina composites with antibacterial properties using sodium alginate as sacrificial template for the development of new biomedical applications. Alumina is a biocompatible and thermally stable ceramic, while silver was chosen for its antibacterial properties (Roque-Ruiz et al. 2018). Another study has reported two different routes for the synthesis of silver-doped anodic alumina nanocomposites with antimicrobial properties using electrochemical deposition and thermal reduction (Kiradzhiyska et al. 2022). Also, an addressed study showed the antimicrobial activity and sorption behavior of alumina/silver nanocomposites.

At the same time, Ag nanoparticles are being intensively researched (Maleki et al. 2015; Baghayeri et al. 2018) due to their unique optical, thermal, electrical, and biological properties (anticancer, antifungal, antiviral, and antibacterial activity). The excellent inhibitory activity of nano silver against many bacteria, including *E. coli*, *M. luteus* (Jagminas et al. 2015), *K. pneumoniae*, and *B. pumilus* (Mokhena and Luyt 2017), is well documented in the literature. Nanoscale species have higher bactericidal activity than microscopic particles, and when they are less than 10 nm in size, they can directly affect cell permeability. The significantly increased surface area of small particles improves the antibacterial activity and bioavailability of biomaterials (Calovi et al. 2021).

The chemical preparation of silver-doped alumina nanostructures with different phase compositions from metal salts has been studied (Zhou et al. 2012; Aparna et al. 2019; Kiseleva et al. 2019; Nasrollahzadeh et al. 2019). Various organic initiators and stabilizers were used to achieve high yield of reaction products and fixation of silver nanoparticles on the alumina surface. Nanostructures with high antibacterial activity were prepared by this method. One of the major drawbacks of chemical synthesis is the different phases and the formation of undesirable byproducts, the removal of which requires further procedures. In addition, the organic stabilizers used are often hazardous. Moreover, the conventional physicochemical processes for nanoparticle synthesis are time-consuming, expensive, require harmful substances, and are not environmentally friendly (Khatami and Iravani 2021). Therefore, the use of plant/plant waste extracts as reducing, capping, and stabilizing agents for the preparation of nanoparticles is more biocompatible and has lower sorption capacity compared to conventionally synthesized nanoparticles (Shameli et al. 2021; Rajoriya et al. 2021). Moreover, these processes are simple and rely on naturally occurring, nontoxic components in the abundant flora

**Scheme 1** General steps of coffee husk extract preparation



in our environment, making the complex syntheses tame (Angulo-Bejarano et al. 2021).

Coffee can be processed either dry or wet, producing a variety of byproducts. Dry processing is the most common process, with the main waste being the husk, which accounts for about 50% of the weight of coffee beans (Tizian et al. 2020). Coffee husks are a rich source of secondary metabolites such as caffeine and tannins, as well as phenolic acids such as chlorogenic acid, making them a promising resource for bioactive components for use in food. Chlorogenic acid is found throughout the plant kingdom, with coffee and its byproducts being the most prolific source (Janissen and Huynh 2018). These phenolic compounds are biologically active and have been associated with their antioxidant, antibacterial, and anticarcinogenic properties (Tungmunnithum et al. 2018).

The search for novel disinfection agents has become a critical topic in light of harmful pathogenic resistance in the water. The constant emergence of bacterial resistance has led researchers to develop new disinfectants. Among the most promising of these agents are metallic nanoparticles, which have shown excellent antibacterial activity in numerous studies. Even when new materials are introduced to the market, antibiotic-resistant bacteria appear in a relatively short time. However, nanoparticles with antibacterial activity are believed to have the potential to minimize or prevent the development of more resistant bacteria because nanoparticles target many biomolecules simultaneously, preventing the formation of resistant strains. Various mechanisms of antibacterial action of different nanoparticles have been reported, including interaction and regulation, ATP deprivation, and membrane interaction (Rahman et al. 2021; Aadir et al. 2021a, 2021b, 2022; Sumra et al. 2022).

Moreover, Dar et al. 2021 synthesized several transition metal oxides at low temperatures and examined their antibacterial efficacy against multidrug-resistant bacterial infections (Dar et al. 2021). Bioactive glass and poly (vinyl alcohol) composites produced by melting and sol–gel methods were recently used as antibacterial materials for disinfection in another study (Maximov et al. 2021; Asadpour et al. 2022).

Metal/oxide nanomaterials, carbonaceous nanomaterials, zeolites, and dendrimers are the most common nanoscale materials used as functional materials for water

decontamination. These materials have a variety of physico-chemical properties that make them attractive for use as separation and reaction media for water treatment (Chakraborty et al. 2021; Jimenez-Reyes et al. 2021).

The aim of this work is to propose a facile synthesis of silver-doped alumina nanocomposite using coffee husks, and the formed nanocomposite was characterized by various microscopic and spectroscopic techniques. The green synthesized silver-doped alumina nanocomposite using coffee husks was used for the first time as an antipathogenic agent for decontamination of wastewater. The antibacterial activity was investigated against two bacterial strains *Escherichia coli* and *Salmonella typhimurium*. The adsorption kinetics and isotherms were also studied.

## Materials and methods

### Chemicals and reagents

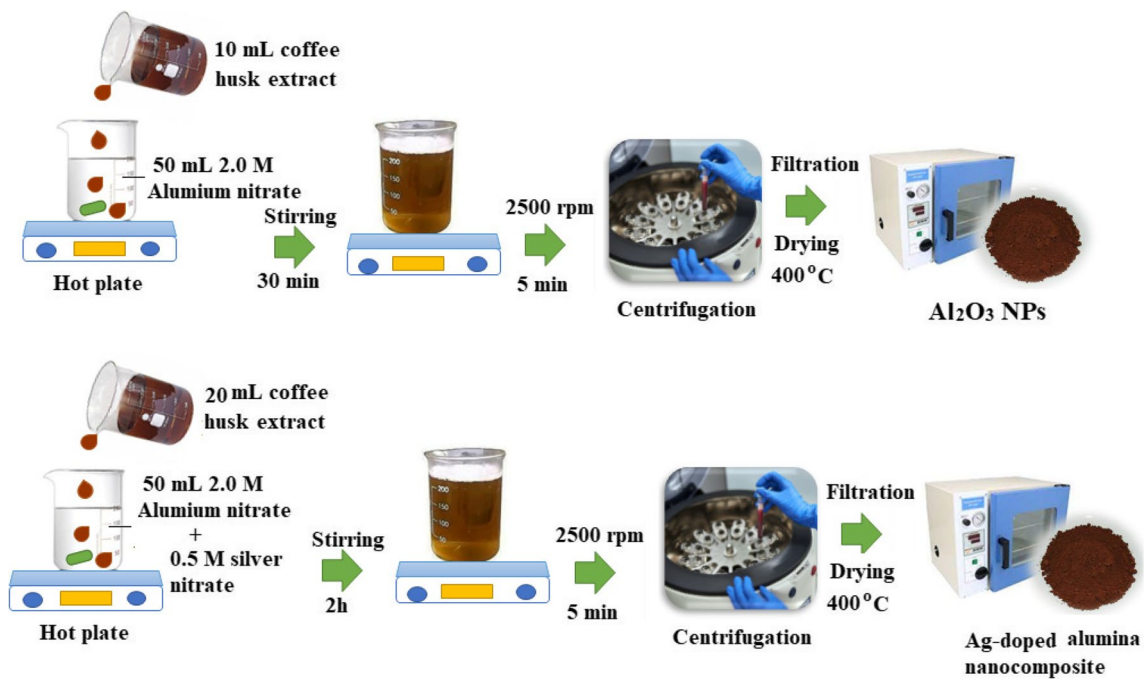
The chemicals aluminum nitrate nonahydrate ( $\geq 98.0\%$ ), ethanol ( $\geq 99.5\%$ ), silver nitrate ( $\geq 99.0\%$ ), and hydroxide sodium (99.9%) were purchased from Sigma-Aldrich (Hamburg, Germany).

### Botanical material

The coffee husks were collected from a local supermarket in Riyadh, Saudi Arabia, in December 2021. The botanical material was identified and authenticated by a taxonomist from the Department of Pharmacognosy at College of Pharmacy, King Saud University. A voucher specimen (CH-0421) was deposited in the same department.

### Preparation of coffee husk extract

Coffee fruit husks were collected, washed thoroughly with deionized water, and air dried for 24 h. About 10 g of coffee husk powder was mixed with 200 mL of deionized water and magnetically stirred at 80 °C for 3 h. The resulting extract was set aside to cool at room temperature. It was centrifuged at 2500 rpm for 5 min and filtered using Whatman No. 41 filter paper. The obtained extract was then stored in a tight container in the refrigerator at 4 °C for further use (Scheme 1).



**Scheme 2** General steps of  $\text{Al}_2\text{O}_3$  NPs and Ag-doped alumina nanocomposite preparation

### Preparation of Ag NPs, $\text{Al}_2\text{O}_3$ NPs, and Ag-doped alumina nanocomposite

To prepare Ag NPs, 20 mL of coffee husk extract was placed in a volumetric flask and heated to 80 °C for 10 min under magnetic agitation (450 rpm). An appropriate amount (100 mL of  $5.0 \times 10^{-3} \text{ mol L}^{-1}$ , 0.0849 g) of silver nitrate solution was added to the heated extract. The pH was optimized to 10 with a few drops of sodium hydroxide ( $0.2 \text{ mol L}^{-1}$ , 0.799 g/100 mL). The brownish color of the mixture showed the conversion of  $\text{Ag}^+$  to  $\text{Ag}^*$  nanoparticles (Zuorro et al. 2022).

Alumina nanoparticles ( $\text{Al}_2\text{O}_3$  NPs) were synthesized green by mixing 10 mL of coffee husk extract with 50 mL of  $2.0 \text{ mol L}^{-1}$  aluminum nitrate nonahydrate (75.028 g/100 mL) under constant magnetic stirring for 30 min. A brownish  $\text{Al}_2\text{O}_3$  precipitate was formed. The formed  $\text{Al}_2\text{O}_3$  NPs were centrifuged at 2500 rpm for 5 min and filtered with Whatman filter paper No. 41. The resulting  $\text{Al}_2\text{O}_3$  NPs were dried and stored in a tight container for further study (Manikandan et al. 2019).

To remove impurities, the precipitated particles were washed two or three times with ethanol. The powder particles were stored in a hot-air oven at 100 °C for one day and then in a muffle furnace at 400 °C for 3 h. Finally, the particles were ground into fine nanoparticles using a mortar and pestle. For the green synthesis of silver-doped alumina nanoparticles, 20 mL of coffee peel extract was mixed with 50 mL of deionized water containing silver nitrate (4.0246 g)

and aluminum nitrate nonahydrate (37.514 g) to produce 0.5 and  $2.0 \text{ mol L}^{-1}$ , respectively. The mixture was stirred magnetically for 2 h. The pH of the mixture was optimized to 12 by adding sodium hydroxide pellets. The formed silver-doped alumina nanoparticles were centrifuged and the same filtration and drying steps as above were performed for the synthesis of alumina nanoparticles (Nasrollahzadeh et al. 2019) (Scheme 2).

### Characterization of $\text{Al}_2\text{O}_3$ NPs and Ag-doped alumina nanocomposite

Spectrophotometric (UV–Vis) characterizations of the synthesized  $\text{Al}_2\text{O}_3$  NPs and Ag-doped alumina nanocomposite were measured using the Ultrospec 2100 biochrom spectrophotometer (Biochrom Ltd., Cambium, Cambridge, UK). Fourier transform infrared spectroscopy (FTIR) (PerkinElmer, Yokohama, Japan) was performed to monitor the surface functional groups of the synthesized  $\text{Al}_2\text{O}_3$  NPs and Ag-doped alumina nanocomposite. The elemental composition of  $\text{Al}_2\text{O}_3$  NPs and Ag-doped alumina nanocomposite was investigated at 20 kV using an energy dispersive X-ray device (EDX, JSM-7610F; JEOL, Tokyo, Japan). Scanning electron microscope (SEM, JEOL Ltd., Tokyo, Japan) and transmission electron microscope (TEM, JEM-1400, JEOL Ltd., Tokyo, Japan) were used to study the surface morphology of the synthesized nanoparticles. The surface morphology of  $\text{Al}_2\text{O}_3$  NPs and Ag-doped alumina nanocomposite was measured using JEM-2100F scanning electron microscope

and JEM-1400 transmission electron microscope (JEOL Ltd., Tokyo, Japan).

### Antibacterial activity

*E. coli* (ATCC 25922) and *Salmonella typhi* (ATCC 14028) were taken from the American Type Culture Collection (ATCC) and used as model pathogens in the current study to measure the antibacterial potential of Ag-doped alumina nanocomposite. The bacterial strains were grown on agar plates and the freshly obtained colonies were inoculated into 100 mL of tryptone-soya broth. Using a UV–vis spectrophotometer, growth was monitored every 4 h until the optical density reached 0.1 at 600 nm (OD of 0.1 corresponded to a concentration of 108 CFU/mL medium). The minimum inhibitory concentration (MIC) of the pre-synthesized Ag-doped alumina nanocomposite was tested by inoculating 1.0 mL of a fully grown culture with 100 mL of a freshly prepared culture broth containing different concentrations (6, 12, 24, and 30  $\mu\text{g mL}^{-1}$ ) of the Ag-doped alumina nanocomposite. Pathogenic cultures were grown under dark conditions and treated with Ag-doped alumina nanocomposite samples as described above. All culture flasks were incubated in a rotary shaker at 37 °C and 150 rpm. Concentration of bacterial strains was determined by optical density (OD) at 600 nm absorbance at 4 h intervals over 16 h using a UV spectrophotometer. *E. coli* and *S. typhi* without the addition of Ag-doped alumina nanocomposite were treated as control samples.

### Determination of bacterial toxicity

The fluorescence staining method was applied to measure the number of dead and live bacteria at specific time intervals using a dead/live BacLight bacterial viability kit. The *E. coli* and *S. typhi* bacterial strains were stained with fluorescent dyes obeying the manufacturer's instructions and were monitored under confocal laser scanning microscopy (CLSM) as previously described (Alovisi et al. 2022).

### Adsorption of Indigo carmine dye on Ag-doped alumina nanocomposite

The batch experiment study was used to evaluate the activity of Ag-doped alumina nanocomposite in removing IGC from water. The effect of contact time and kinetics study were performed by treating 200 mL of IGC dye solution (160  $\text{mg L}^{-1}$ ) with 85 mg of Ag-doped alumina as sorbent under continuous stirring. Then, 10 mL of the reaction mixture was withdrawn and filtered, and the absorbance of IGC was recorded by UV–vis spectroscopy. The adsorption capacity in each time interval was calculated using Eq. (1), and the best sorbent was selected for further study.

$$q_t = \frac{(C_0 - C_t) \times V}{M} \quad (1)$$

where  $C_0$  and  $C_t$  represent the IGC dye concentration ( $\text{mg L}^{-1}$ ) at zero and  $t$  time, and  $V$  and  $M$  represent the volume (L) IGC dye solution and mass (g) of sorbent Ag-doped alumina nanocomposite, respectively.

The results obtained were applied to evaluate the adsorption kinetics of IGC. Pseudo 1<sup>st</sup> order model (FOM) and 2<sup>nd</sup> order model (SOM) kinetics were used to estimate the sorption rate by applying Eqs. (2) and (3).

$$\ln(q_e - q_t) = \ln(q_e) - k_1 \times t \quad (2)$$

$$\frac{1}{q_t} = \frac{1}{k_2 q_2 2t} + \frac{1}{q_e} \quad (3)$$

However, the step involved in controlling adsorption, intra-particles model (IM), and liquid film model (LM) diffusion was analyzed by applying Eqs. (4) and (5).

$$q_t = K_{IM} \times t^{1/2} + C_i \quad (4)$$

$$\ln(1 - F) = -K_{LM} \times t \quad (5)$$

where  $K_1$  and  $K_2$  represent the rate constant of FOM ( $\text{min}^{-1}$ ) and SOM ( $\text{g mg}^{-1} \text{min}^{-1}$ );  $K_{IM}$  ( $\text{mg g}^{-1} \text{min}^{-0.5}$ ) and  $K_{LM}$  ( $\text{min}^{-1}$ ); the IM and LM are constants, the  $q_e$  and  $C_i$  represent the equilibrium adsorption capacity ( $\text{mg g}^{-1}$ ) and boundary layer thickness ( $\text{mg g}^{-1}$ ) parameters.

In addition, IGC adsorption on the Ag-doped alumina nanocomposite was investigated at different pH values. The IGC solution (160  $\text{mg L}^{-1}$ ) was adjusted to a pH between 2 and 10. Two hundred milliliters of the optimized IGC solution was treated with 85 mg of the Ag-doped alumina nanocomposite under constant stirring until equilibrium, and the remaining reaction mixture was used as a reference standard.

### Adsorption equilibria

The effect of the initial concentration of IGC on its removal by the good sorbent was studied using different IGC concentrations (40, 80, 120, and 160  $\text{mg L}^{-1}$ ), and the effect of temperature on IGC removal was studied at different temperatures (30, 40, and 50 °C). The obtained results were used to analyze the sorption isotherms and thermodynamics.

### Application to natural water samples

The seawater sample was collected from the coast of Jeddah, Saudi Arabia. The water sample was mixed with an appropriate amount of IGC solution (160  $\text{mg L}^{-1}$ ) to obtain a concentration of 10  $\text{mg L}^{-1}$ . The contaminated seawater

was treated with 85 mg Ag-doped alumina nanocomposite under constant stirring at room temperature, and the removal efficiency of the nanocomposite was evaluated by applying Eq. (6).

$$\%E = \frac{(C_0 - C_t) \times 100}{C_0} \quad (6)$$

### Statistical analysis

The statistical analysis of the current study was carried out by ANOVA using SPSS software version 19.0. with numerous comparisons and the least significant difference.

## Results and discussion

Recently, most natural water reservoirs have high levels of pathogenic bacterial contamination, and consumption of this contaminated water is the main cause of various diseases that are widespread in developing countries (Kristanti et al. 2022). Nanomaterials with interesting properties have revealed new ways to improve waste treatment techniques. These techniques often involve coating pollutants to reduce the toxicity of constituents and kill pathogens, as well as cleaning contaminants from water due to the reactive surfaces of smart materials. Therefore, the development of such antibacterial nanomaterials is of great importance for the development of water purification systems.

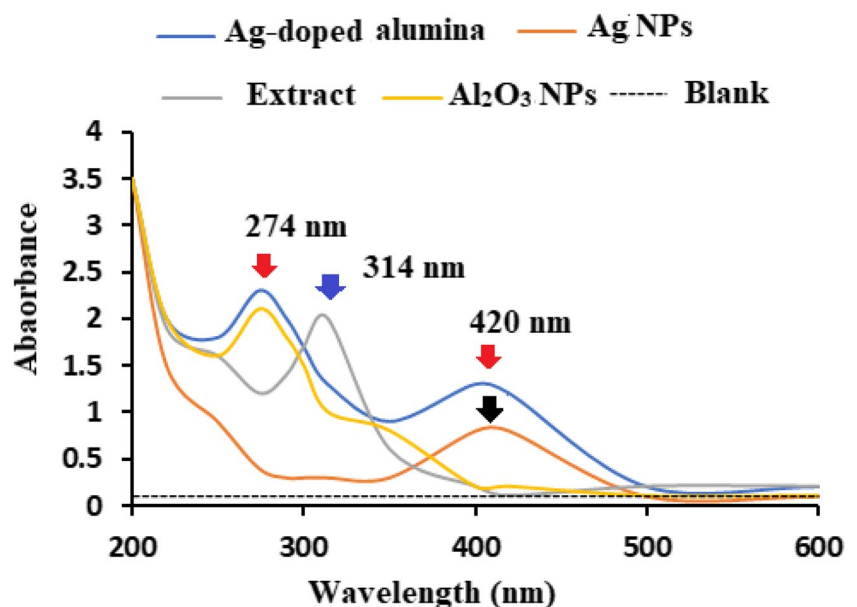
In the current study, well-developed  $\text{Al}_2\text{O}_3$  NPs and Ag-doped alumina nanocomposites were synthesized by a green approach using coffee husk waste. The  $\text{Al}_2\text{O}_3$  NPs

were prepared by mixing coffee husk extract with aluminum nitrate under continuous magnetic stirring. The Ag-doped alumina nanocomposite was prepared by combining equimolar amounts of coffee husk extract with aluminum nitrate and silver nitrate under constant magnetic stirring. The experimental conditions such as duration, temperature, and appropriate pH suitable for obtaining consistent Ag-doped alumina nanocomposite-like morphology were set as 2 h, 25 °C, and pH 12. The morphological characteristics showed the pre-synthesized metal oxide and nanocomposite. Identification and characterization of the formed  $\text{Al}_2\text{O}_3$  NPs and Ag-doped alumina nanocomposite were carried out using various spectroscopic and microscopic techniques.

### Characterization

The optical behavior of the Ag NPs,  $\text{Al}_2\text{O}_3$  NPs, and Ag-doped alumina nanocomposite prepared with coffee husk extract was investigated by UV–vis spectroscopy. The coffee husk extract showed an absorption peak at 314 nm in the UV region. The synthesized Ag NPs exhibited remarkable optical properties, which were directly attributed to the surface plasmon resonance (SPR) absorption peak at 420 nm, resulting from the reduction of silver ions to silver nanoparticles. The observed broad peak of Ag NPs can be explained by the formation of polydisperse in the prepared sample (Yang et al. 2010). However, for  $\text{Al}_2\text{O}_3$  NPs and Ag-doped alumina nanocomposite, two distinct absorption peaks were recorded at 274 and 420 nm (Fig. 1). Moreover, the nanoparticles exhibited comparatively high stability even after 2 weeks, as evidenced by the negligible changes in their absorption peak. This stability is likely due to the presence of antioxidants and phenolic compounds in the coffee husk extract, which

**Fig. 1** Optical behavior (UV–Vis) absorbance spectra of Ag-doped alumina nanocomposite, Ag NPs, extract,  $\text{Al}_2\text{O}_3$  NPs, and blank



protect the nanoparticles from deformation and decomposition (Ribeiro et al. 2019).

The band gaps of the synthesized Ag NPs, Al<sub>2</sub>O<sub>3</sub> NPs, and Ag-doped alumina nanocomposite were calculated using the following relationship:

$$\text{Energy quantum mechanics } E_g = hc/\lambda \quad (7)$$

where the values of  $h$ ,  $C$ , and  $\lambda$  represent the expressed bank constant ( $6.626 \times 10^{-34}$  J.s), the speed of light ( $2.99 \times 10^8$  m/sec), and the absorption peak, respectively. The estimated values of the band gap were given as 2.95 eV, 4.52 eV, and 3.87 eV, respectively, for the above nanomaterials. The reduced shape of the surface is due to surface plasmon resonance (SPR), which also increases the scattering probability and penetration of radiation. These mechanisms, which include the creation of holes on the surface and the separation of electrons, accelerate the oxidation process. In addition, it has been demonstrated that changes to the dielectric matrix can affect the absorption peak that appears on an SPR. It is known that the refractive index of the matrix is directly related to its effective dielectric behavior.

The FT-IR technique provides the probable functional groups present in biomolecules that may be responsible for the reduction process to nanoparticles, capping, and stabilization of the synthesized nanostructures. The spectrum of the coffee shell FT-IR (Fig. 2 a) shows two bands at 1058 and 777 cm<sup>-1</sup> due to the presence of polysaccharides, as previously reported in the literature (Cangussu et al. 2021),

where 1250–700 cm<sup>-1</sup> represents the fingerprint region of polysaccharides. The broad band at 3425 cm<sup>-1</sup> expresses the intermolecular O–H bond of the alcohol or the average N–H stretching vibration of the primary amine. The two prominent low absorption bands at 2926 and 2847 cm<sup>-1</sup> express the C–H stretching vibration of the methyl group of the caffeine molecule (Cruz et al. 2013). The spectrum of the coffee husk sample also showed increased wavenumber values between 1700 and 1500 cm<sup>-1</sup>. The bands in this region (1621 and 1437 cm<sup>-1</sup>) can be attributed to the axial deformation of the C=C and C=N bonds in the aromatic ring of trigonelline (Reis et al. 2013). The FT-IR spectrum of Ag NPs (Fig. 2 a) shows two bands, one broad around 3405 cm<sup>-1</sup> and others at 2923 and 2370 cm<sup>-1</sup>, attributed to the O–H (aromatic or aliphatic alcohol), the average C–H stretching vibration of the alkane, and strong N–H stretching of amine salt, respectively. The observed bands (Fig. 2 b) at 1706 and 1605, 1446, 756, 695, and 536 cm<sup>-1</sup> are attributed to the strong C=O stretching of the carboxylic acid, the mean C=C stretching of the conjugated alkene, the mean O–H bending of the carboxylic acid, the trisubstituted C=C of the alkene, the strong halogen compound, and the Ag NPs, respectively (Aadil et al. 2020).

Figure 2 c shows the functional groups formed during the synthesis of Al<sub>2</sub>O<sub>3</sub> NPs from coffee husk extract. The recorded bands at 3465, 2444, 1636, 1359, 1052, 834, and 618 cm<sup>-1</sup> express the presence of strong intermolecular bonds of alcoholic O–H stretching vibrations, weak S–H stretching vibrations of thiol groups, medium strength C=C

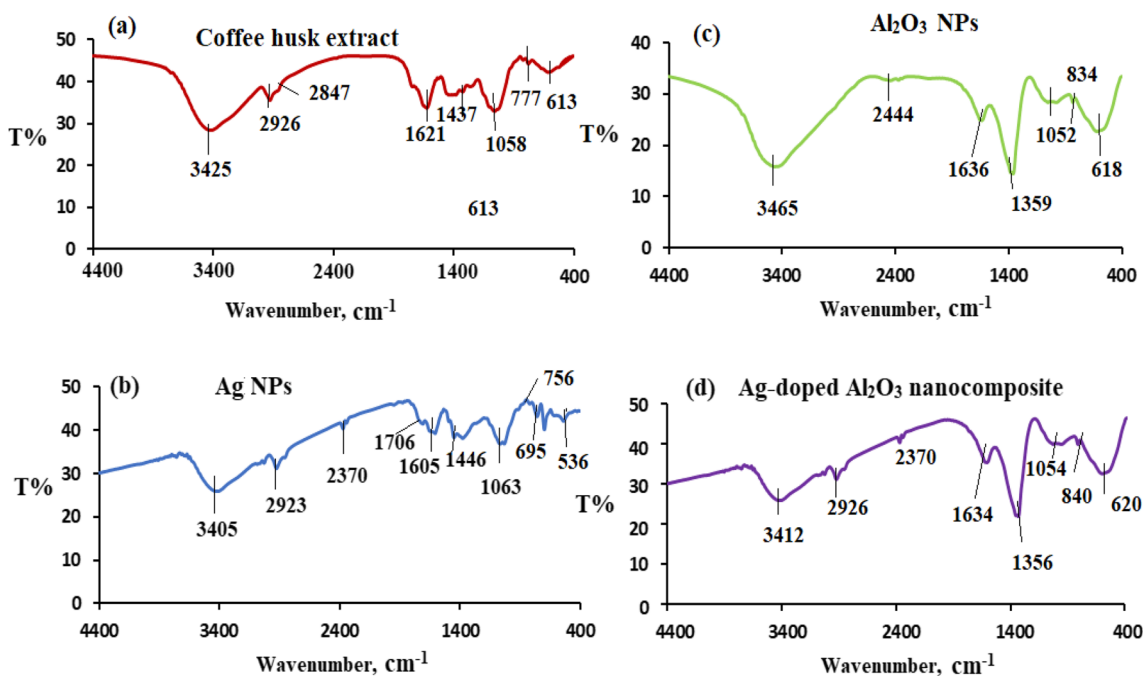


**Fig. 2** FT-IR findings for **a** coffee husk extract, **b** Ag NPs, **c** Al<sub>2</sub>O<sub>3</sub> NPs, and **d** Ag-doped alumina nanocomposite

stretching vibrations of disubstituted alkenes, medium strength C–H bending vibrations of alkanes, strong C–O stretching vibrations of alkyl aryl ethers, and strong halogen compounds and Al–O nanoparticles, respectively. The functional groups observed in Fig. 2 d showed combined functional groups of Ag and Al–O spectra, indicating the formation of Ag-doped alumina nanocomposite.

The XRD spectrum was utilized to study the crystalline nature of the pre-synthesized nanomaterials. As demonstrated in Fig. 3 a, the XRD spectrum showed the crystallite nature of Ag NPs which displayed five remarkable peaks at 38.13° (1 1 1), 46.12° (2 0 0), 54.55° (1 4 2), 67.74° (2 2 2), and 76.84° (3 1 1) crystalline planes, respectively. These values were in agreement with the indexed values of JCPDS. No. 04–0783 of Ag NPs and revealed the crystalline structure of the synthesized Ag NPs (Feret et al. 2000). The XRD spectrum of Al<sub>2</sub>O<sub>3</sub> NPs was also studied to explain their crystalline nature (Fig. 3 b).

Different observed peaks were recognized at 29.49° (0 1 2), 35.48° (1 0 4), 38.99° (1 1 0), 42.62° (1 1 3), 55.69° (0 2 5), 59.94° (1 1 6), 66.76° (2 1 4), and 68.73° (3 0 0) crystalline planes. The recorded values well matched the standard JCPDS card No. 46–1212 of Al<sub>2</sub>O<sub>3</sub> NPs (Holzwarth and Gibson 2011). Furthermore, the XRD spectrum of Ag-doped alumina nanocomposite showed the presence of three significant peaks of Ag corresponding to (2 0 0), (2 2 0), and (3 1 1) crystalline planes revealing the formation of Ag-doped alumina nanocomposite (Fig. 3 c). The average crystallite size of the pre-formed nanomaterials was estimated from the Debye-Scherrer equation (Song et al. 2013):

$$\text{Average crystallite size } D = 0.94\lambda/\beta\cos\theta \tag{8}$$

where these values are *D* (the average crystallite size),  $\lambda$  (the absorption wavelength, 1.54056 Å for Cu K $\alpha$  radiation),  $\beta$  (the width of the peak at ½ maximum intensity), and  $\theta$  (the peak position angle), respectively. The average estimated crystallite size of Ag NPs, Al<sub>2</sub>O<sub>3</sub> NPs, and Ag-doped alumina nanocomposite was 17.3 ± 4.2, 19.2 ± 2.4, and 23.9 ± 1.1 nm, respectively. The absence of any additional peaks related to other elements confirmed the high purity of the synthesized nanomaterials.

Cell length (*a* & *c*), volume (*V*), x-ray density ( $\rho_{x\text{-ray}}$ ), total density ( $\rho_m$ ), and porosity (%) were calculated using the Cell Software. All these parameters were estimated using Eqs. 9–12 (Bibi et al. 2021; Touqeer et al. 2020; Aamir et al. 2021; Kousar et al. 2022) and the results are shown in Table 1.

$$\text{Cell volume} = a^2 \times c \times 0.866 \tag{9}$$

$$\rho_{x\text{-ray}} = \frac{Z \times M}{V_{\text{cell}} \times N_A} \tag{10}$$

$$\rho_m = \frac{m}{\pi r^2 \times h} \tag{11}$$

$$\text{Porosity (\%)} = 1 - \frac{\text{Bulk density}}{x\text{-ray density}} \tag{12}$$

After co-doping, the unit cell volume decreased from 68.31 × 10<sup>−24</sup> cm<sup>3</sup> to 52.14 × 10<sup>−24</sup> cm<sup>3</sup>, while the X-ray

**Fig. 3** XRD patterns of pre-synthesized **a** Ag NPs, **b** Al<sub>2</sub>O<sub>3</sub> NPs, and **c** Ag-doped alumina nanocomposite using coffee husk extract

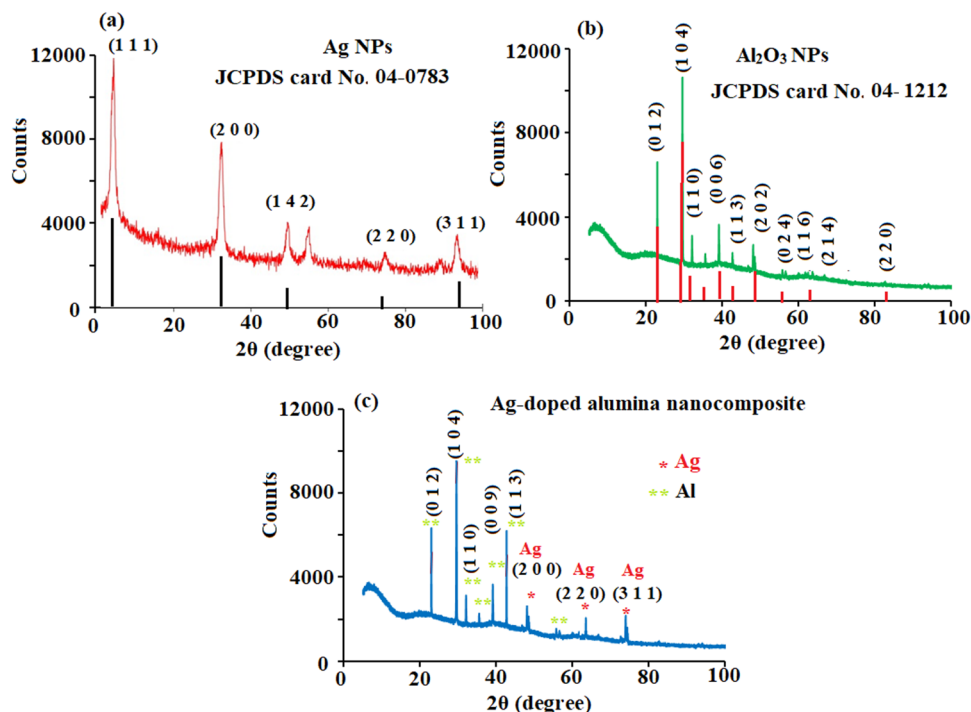




**Table 1** Cell parameters of Ag NPs, Al<sub>2</sub>O<sub>3</sub> NPs, and Ag-doped alumina nanocomposite

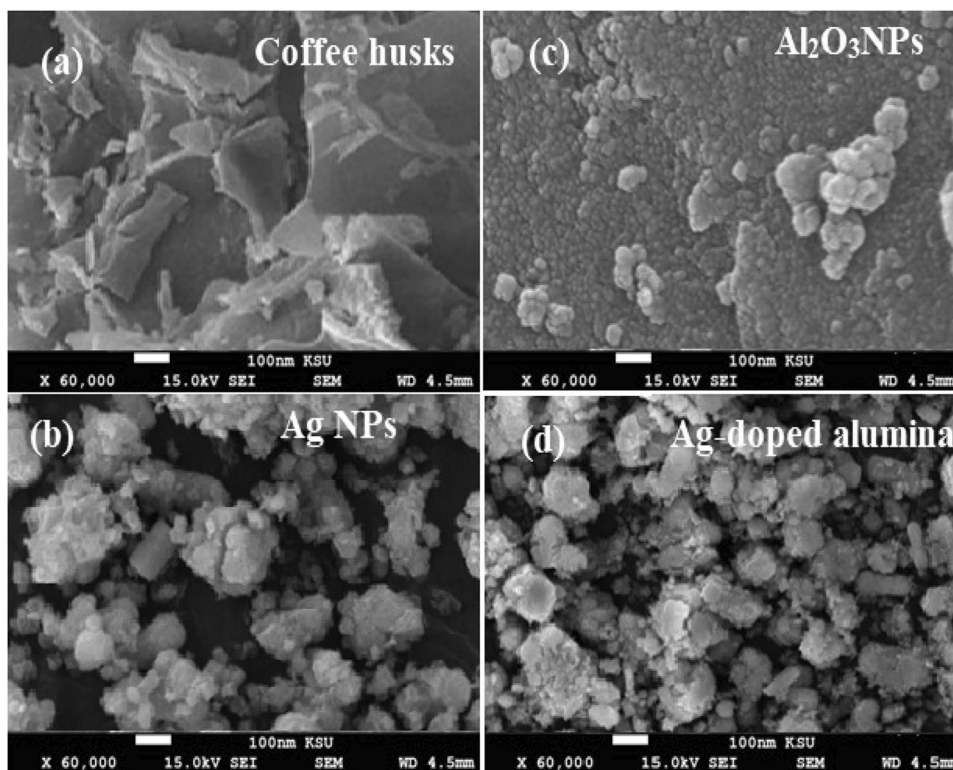
Parameters	Ag	Al <sub>2</sub> O <sub>3</sub>	Ag-doped alumina
Lattice constant a/Å	4.079	7.941	6.452
Cell volume /cm <sup>3</sup>	68.31 × 10 <sup>-24</sup>	66.62 × 10 <sup>-24</sup>	52.14 × 10 <sup>-24</sup>
Bulk density (g/cm <sup>3</sup> )	10.49	15.22	12.47
x-ray density (g/cm <sup>3</sup> )	27.12	33.86	58.43
Porosity (%)	61.32	55.00	78.65
Crystallite size (nm)	17.3	19.2	23.9

density increased from 27.12 to 58.43 g/cm<sup>3</sup>. This could be due to the replacement of smaller host cations by larger cations caused by the expansion of the unit cell. The porosity of the prepared materials ranged from 61.32 to 78.65%, which is consistent with previous results.

One of the most popular tools for characterizing nanomaterials and nanostructures is the scanning electron microscope (SEM). The signals resulting from the interactions between electrons and the sample provide details about the sample, such as its chemical composition and surface appearance. SEM was used to study the morphology of fine coffee husk powder (Fig. 4 a). The acquired image show that the coffee husk has an uneven surface with particle size in

the range of 0.5–100 μm (Lanje et al. 2010). SEM was used to assess the shape of Al<sub>2</sub>O<sub>3</sub> NPs. The results of the SEM examination used to evaluate the morphology are shown in Fig. 4 b. The nanoparticles were hemispherical in shape and had an average size of 80 nm. The SEM image of the Ag NPs synthesized from coffee husk extract showed relatively spherical nanoparticles. The particle size of the synthesized Ag NPs was about 50 nm (Fig. 4 c). The surface morphology of the Ag-doped alumina showed spherical, non-uniformly distributed particles. The large particle size of about 100 nm was due to the agglomeration of the crystallites (Fig. 4 d). The gray-white mass indicated the successful diffusion of the silver metal on the surface of the Al<sub>2</sub>O<sub>3</sub> NPs.

The elemental composition and mapping of the synthesized Ag NPs, Al<sub>2</sub>O<sub>3</sub> NPs, and Ag-doped alumina nanocomposites were determined using SEM in conjunction with an EDX spectrometer. The results showed the presence of two peaks between 3 and 4 kV associated with the characteristic Ag lines K and L with a weight fraction of 71.36% and an atomic fraction of 37.99%, respectively. The maxima observed at 0.2 kV and 3.6 kV correspond to C and Cl with a weight fraction of 16.42% and 12.22%, respectively, and an atomic content of 35.13% and 28.88%, respectively. The presence of carbon could be due to the presence of stabilizers with alkyl chains (Puchalski et al. 2007). The presence of a weak chlorine peak is attributed to phytochemicals that may be present in the coffee husk and are undoubtedly functionalized on the synthesized AgNPs (Fig. 5 a).

**Fig. 4** SEM images of a coffee husk powder, b Ag NPs, c Al<sub>2</sub>O<sub>3</sub> NPs, and Ag-doped alumina nanocomposite

The EDX spectrum of Al<sub>2</sub>O<sub>3</sub> NPs displayed the presence of four recognized peaks related to Al with wight% 17.46 and atomic % 10.46%. Furthermore, two strong peaks were observed at 0.2 and 0.4 kV related to C and O, respectively. The estimated weight% was 18.49% and 64.06%, and atomic% 24.87% and 64.06%, respectively (Fig. 5 b). The EDX of Ag-doped alumina nanocomposite showed the presence of two peaks between 3 and 4 kV corresponding to Ag with weight% 13.95% and atomic % 9.25%. Additionally, three peaks were noticed at 1.5, 1.9, and 5.5 kV attributed to Al with a weight% of 31.85% and atomic% of 9.93%. These peaks confirmed the successful formation of Ag-doped alumina nanocomposite. Moreover, two remarkable peaks were recorded at 0.2 and 0.4 kV related to C and O with weight% of 28.65%, 36.38%, and atomic% of 44.81%, and 35.74, respectively (Fig. 5 c). Furthermore, the synthesized Ag NPs, Al<sub>2</sub>O<sub>3</sub> NPs, and Ag-doped alumina nanocomposite using coffee husk extract were also investigated by elemental mapping. The results revealed the good distribution of the formed nanomaterials (Figs. 6 a, c).

### Antibacterial activity

The WHO defines safe drinking water as water with a theoretical microbial load of zero. Water supply can be improved through good sanitation, resource management, and hygiene. In addition, it is believed that improving water quality can help prevent 10% of all infections worldwide. In this context, nanotechnology has recently increased the potential for safe water purification techniques. The antibacterial potential of Ag-doped alumina nanocomposite was investigated against *E. coli* and *S. typhi*, two Gram-negative bacterial strains. The growth rate was measured at regular intervals based on OD. In the current study, optimal growth was achieved during the log phase, which lasted 4–12 h. Thereafter, the rate of doubling phase decreased and a stationary phase was observed in both *E. coli* and *S. typhi* control cells. Five different concentrations of the Ag-doped alumina nanocomposite were used to test the antibacterial potential. The minimum inhibitory concentration of the Ag-doped alumina nanocomposite was found to be 12 µg mL<sup>-1</sup> for antibacterial activity (Fig. 7 a–b), and as the concentration of the nanocomposite

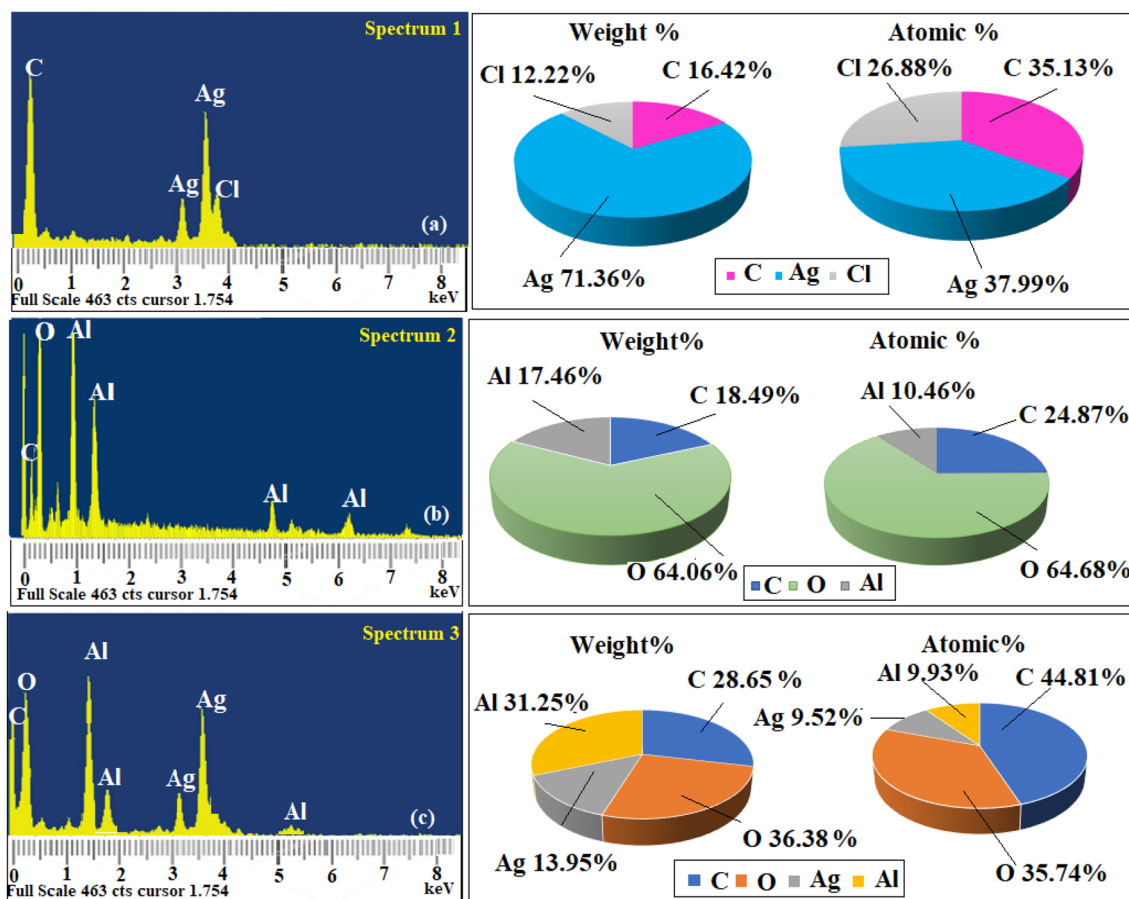
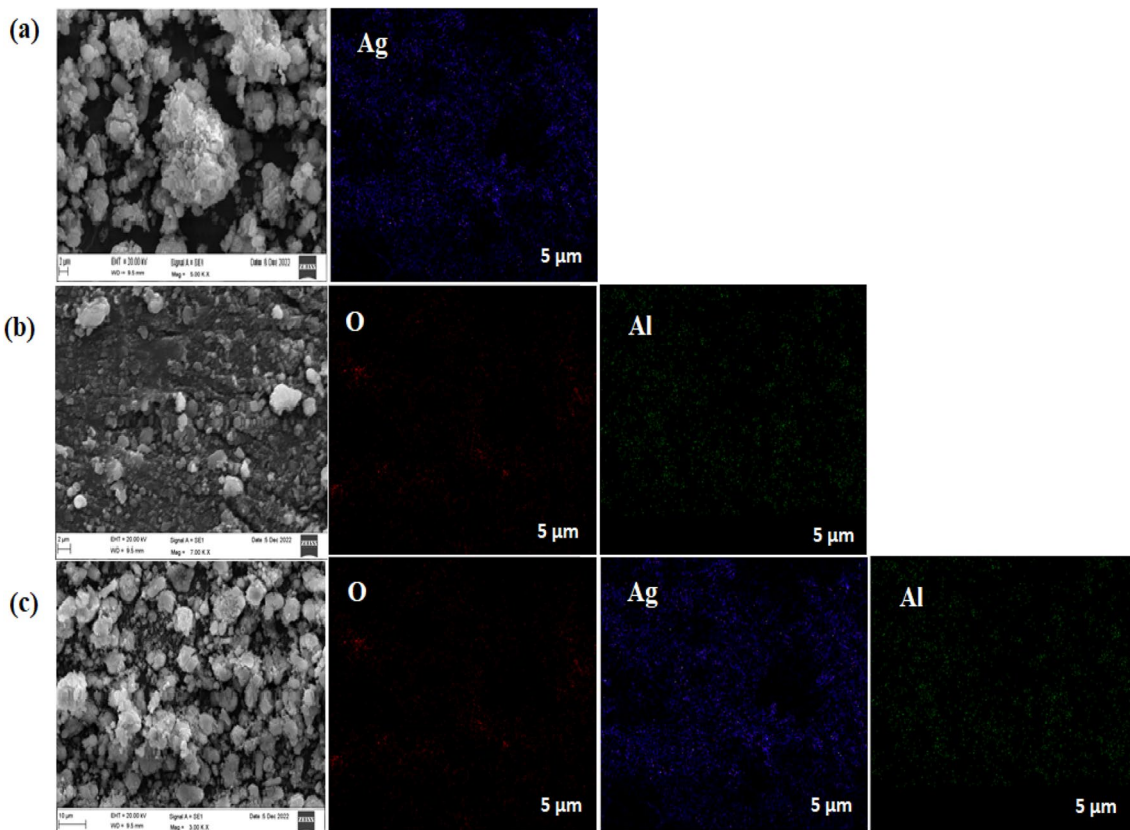


Fig. 5 EDX spectrum of a Ag NPs, b Al<sub>2</sub>O<sub>3</sub> NPs, and c Ag-doped alumina nanocompoiste prepared from coffee husk extract



**Fig. 6** Elemental mapping of **a** AgNPs, **b** Al<sub>2</sub>O<sub>3</sub>NPs, and **c** Ag-doped alumina nanocomposite

increased, the inhibition also increased. Significant inhibition was observed at a concentration of 30  $\mu\text{g mL}^{-1}$  for both bacterial strains. However, inhibition was higher for *E. coli* (Fig. 7 a) than for *S. typhi* (Fig. 7 b).

It is interesting to note that the Ag-doped alumina nanocomposite showed antibacterial effect on *E. coli* and *S. typhi* cells even under dark conditions. However, the antibacterial effect was low under dark conditions with similar concentrations for both pathogenic strains. Moreover, the highest concentration (30  $\mu\text{g mL}^{-1}$ ) had the most deleterious effect on *E. coli* cells. Our results suggest that contact time and concentration influence the inhibitory effect. The exposed bacterial cells were stained with fluorescent dyes to gain insight into cell death, as these dyes are specific for nucleic acids. The kit included SYTO9 and propidium iodide dyes (PI). The representative CLSM images of *E. coli* and *S. typhi* before and after staining are shown in Figs. 7 c–e and d–f.

The green fluorescence of SYTO9 is able to penetrate all cells and was used to assess total cell number (Figs. 7 c and e), whereas the red fluorescence of PI penetrates only cells with disrupted cytoplasmic membranes (Figs. 7 d and f). Living cells are impermeable to dyes such as PI because their membranes are intact. It is clear from the CLSM images that only dead *E. coli* and *S. typhi* cells were

observed at a higher concentration of the Ag-doped alumina nanocomposite (30  $\mu\text{g mL}^{-1}$ ). Once again, it was proved that toxicity depends on contact time and concentration. The harmful effects of nanomaterials on biological systems need to be understood by biomedical sciences. The main causes of bacterial toxicity of nanomaterials can be explained on the basis of membrane and oxidative stress, as described in the literature already available (Ezealigo et al. 2021).

Membrane stress was caused by direct contact between the Ag-doped alumina nanocomposite and the selected bacteria, ultimately leading to destruction of the bacterial cell wall and cell death (Godoy-Gallardo et al. 2021). The antibacterial effect of silver nanomaterials has been reported previously, and the authors theorized a possible mechanism. According to their study, silver nanoparticles were dispersed in a liquid medium, and Ag<sup>+</sup> ions interacted with and accumulated in the walls of bacterial cells (Ekrikaya et al. 2021). In the current study, there is a possibility of a photocatalytic effect in which reactive radicals are generated after being exposed to visible light. The Ag-doped alumina nanocomposite continuously interacted with bacterial cells, exerting remarkable toxicity against the selected *E. coli* and *S. typhi*. The OD was recorded as a function of time, as shown in Figs. 7 a and b. The deleterious effect of the

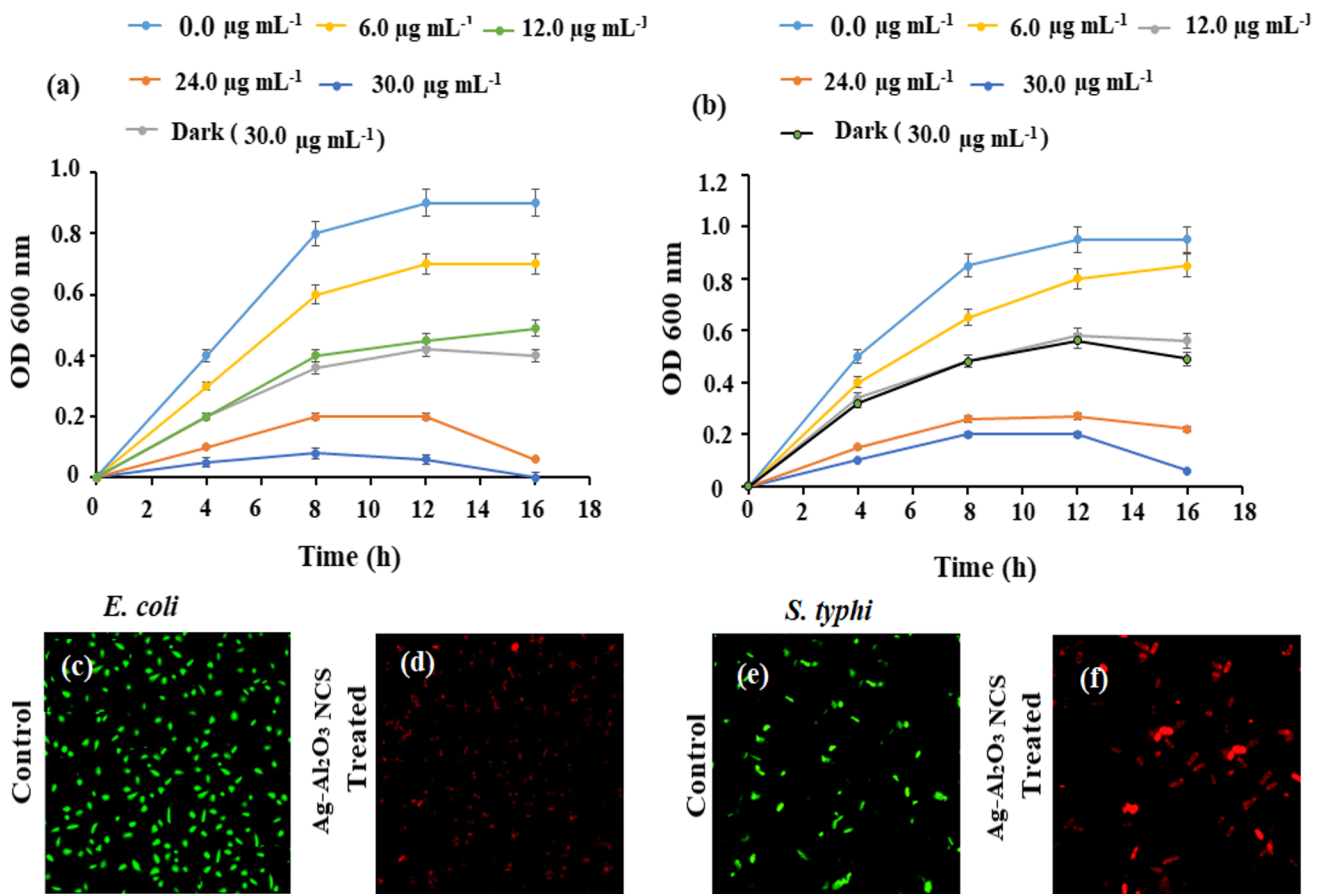


**Fig. 7** Kinetic growth of *E. coli* cells and *S. typhi* a exposed to different concentrations of Ag-doped alumina nanocomposite NCS. The experiments were performed three times and a difference was estimated to be significant statistically at  $p < 0.05$  value. SPSS-19.0 statistical software was used for statistical computations. At all the selected concentrations (6, 12, 24, and 30  $\mu\text{g mL}^{-1}$  (light),

30  $\mu\text{g mL}^{-1}$  (dark), the OD values were significant at  $p < 0.05$  value. The OD value for all the abovementioned concentrations was significant at a value  $p < 0.05$  d and f at the culture time of 12 and 16 h. Representative CLSM images of c *E. coli* and e *S. typhi* control cells treated with to Ag-doped alumina nanocomposite (30  $\mu\text{g mL}^{-1}$ )

nanocomposite on selected bacteria was further illustrated by CLSM images. Figures 7 c, e, d, and f show that *E. coli*, *S. typhi*, nanocomposite treated *E. coli*, and nanocomposite treated *S. typhi* have higher concentration.

This is how the plausible plot technique is described. It was hypothesized that the Ag-doped alumina nanocomposite adhered to the outer cell membrane of the bacterium, which eventually led to cell lysis after the cell was further broken. However, the Ag-doped alumina nanocomposite first adhered to the outer cell wall and then penetrated the inner cell membrane, damaging the cell membrane and allowing the disorganized intracellular contents to leak out and completely destroy the bacterial cell. In Gram-negative bacteria such as *E. coli* and *S. typhi*, there is only a thin layer of peptidoglycan between the cytoplasmic membrane and the outer membrane. It is believed that the  $\text{Ag}^+$  atoms in the Ag-doped alumina nanocomposite interact with the bacterial cells and attach to the bacterial cell walls when the Ag-doped alumina

nanocomposite is dispersed in the medium. This is due to the excess of carboxyl and other groups that dissociate at biological pH and negatively charge the surface of the bacterial cells (Zhao et al. 2022). The opposite charges of the bacteria and  $\text{Ag}^+$  atoms in the Ag-doped alumina nanocomposite and the electrostatic forces could be the cause of their adhesion and bioactivity. Thus, the free radicals and electrostatic forces are most likely the reason for the harmful effect of the Ag-doped alumina nanocomposite in the current study. Thus, the result of the study is that the formed Ag-doped alumina nanocomposite is a potential candidate for use as an antibacterial agent for wastewater treatment.

### Effect of surface morphology

The surface and porosity properties of the Ag-doped alumina nanocomposite were determined by analyzing the  $\text{N}_2$  adsorption–desorption isotherm (Fig. 8 a). The

Barrett-Joyner-Halenda (BJH) method was used to measure the pore diameter and volume, while the surface area was measured by the Brunauer–Emmett–Teller method (BET). The Ag-doped alumina nanocomposite showed H3-type loop hysteresis with cylindrical pores associated with slit-like non-rigid aggregate particles. The Ag-doped alumina nanocomposite showed the highest surface area in the BET technique, which was confirmed by the SEM results showing that the formed nanocomposite has the best adsorption capabilities (Table 2).

### IGC adsorption estimation

The effect of contact time on IGC adsorption of Ag-doped alumina nanocomposite is shown in Fig. 8 b. Although adsorption equilibrium did not develop in the first 3 h, a total of 92% of the adsorbed substances were adsorbed in the first 50 min. The  $q_t$  value obtained for the Ag-doped alumina nanocomposite was 197.6 mg g<sup>-1</sup>. These results are consistent with the high surface area obtained by the BET estimation of the Ag-doped alumina nanocomposite.

### Effect of pH

The effect of pH on the removal of IGC by Ag-doped alumina nanocomposites is shown in Fig. 8 c. At low pH, IGC sorption was decreased, and it was even more decreased in

**Table 2** The surface features of the formed Ag-doped alumina nanocomposite

Sample name	BET surface area m <sup>2</sup> g <sup>-1</sup>	Average pore diameter (Å)	Average pore volume cm <sup>3</sup> g <sup>-1</sup>
Ag-doped alumina nanocomposite	126.58	145.95	0.45

the high pH solution. The performance of the Ag-doped alumina nanocomposite remained constant in the pH range from 5 to 8, with pH 6 being preferred. The reason may be due to the molecular structure of IGC, which contains a high concentration of H<sup>+</sup> ions that can protonate the electron-rich sites of the ionic dye and lead to the repulsion of some sites of the metal oxide nanoparticles. In this way, the electron-rich sites are occupied, which reduces the availability of the dye and participates in the sorption process. As a result, the -OH groups can occupy the active sorption sites of the sorbent at higher pH (Elamin et al. 2023).

### Adsorption kinetics

The adsorption order and rate control mechanism for IGC dye adsorption were evaluated on the surface of Ag-doped alumina nanocomposite. The  $R^2$  values for IGC sorption were 0.9923 at a  $K_1$  value of 0.043 min<sup>-1</sup> and 0.9336 at a

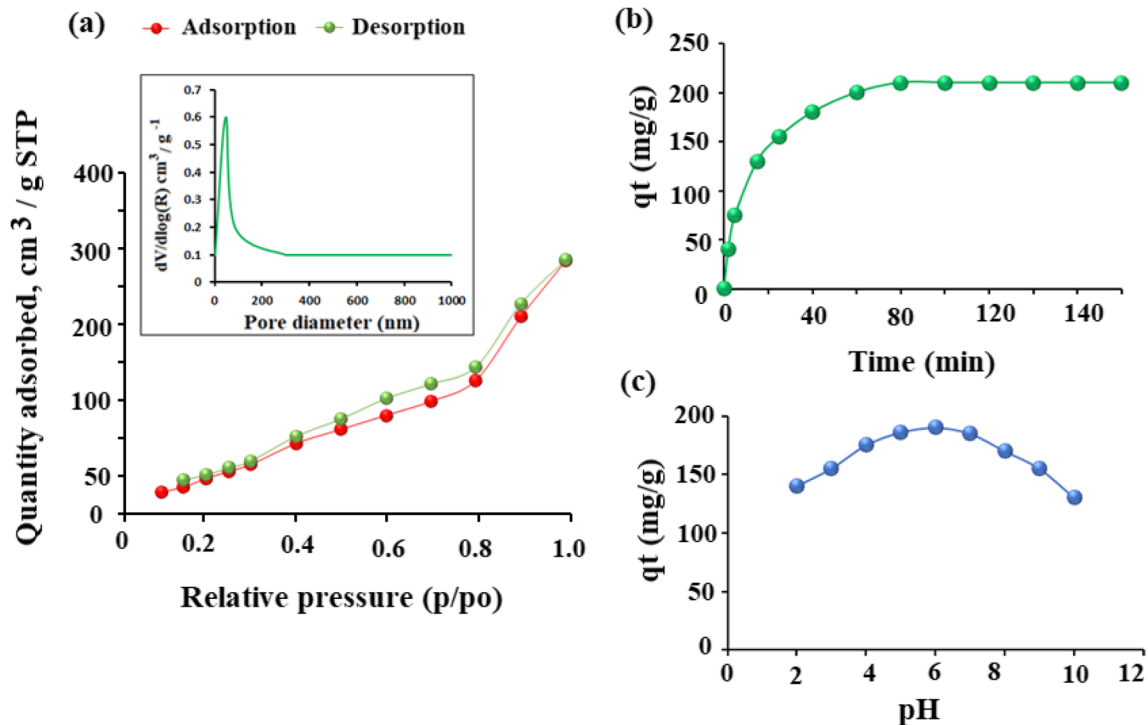


**Fig. 8** a N<sub>2</sub> adsorption isotherm and pore size distribution, b contact time of IGC removal, and c effect of pH on the IGC removal by Ag-doped alumina nanocomposite

$K_2$  value of  $0.008 \text{ g mg}^{-1} \text{ min}^{-1}$  for FOM and SOM, respectively. However, evaluation of the rate control mechanism yielded  $R^2$  values of 0.9962 with an equilibrium constant of  $0.034 \text{ mg g}^{-1} \text{ min}^{-0.5}$  and 0.9852 with an equilibrium constant of  $16.23 \text{ min}^{-1}$  for LDM and IM, respectively (Figs. 9 a, c). The obtained results indicate that the sorption of IGC dye on the surface of Ag-doped alumina nanocomposite is by FOM and the sorption is controlled by LDM (An 2020). Following the FOM and LDM mechanism indicates that the particle size of Ag-doped alumina nanocomposite is small and has high affinity for IGC dye removal (Hameed and El-Khaiary 2008).

**Adsorption isotherms**

The adsorption isotherms were studied using the results from the effect of concentrations. The models of Langmuir (LIM) and Freundlich (FIM) were applied to study the adsorption probabilities of monolayers and multilayers corresponding to Eqs. (13) and (14).

$$\frac{1}{q_e} = \frac{1}{K_L q_m} \cdot \frac{1}{C_e} + \frac{1}{K_L} \tag{13}$$

$$\ln q_e = \ln K_F + \frac{1}{n} \ln C_e \tag{14}$$

$K_L, C_e, q_m, q_t, K_F,$  and  $1/n$  represent the constant LIM ( $\text{Lmg}^{-1}$ ), the concentration of the equilibrium solution ( $\text{mg L}^{-1}$ ), the estimated maximum ( $\text{mg g}^{-1}$ ), the equilibrium constant ( $\text{L mg}^{-1}$ ), and the heterogeneity factor of FIM, respectively. The plots of LIM and FIM are shown in Figs. 10 a and b, and the calculated results are given in Table 3. The adsorption of IGC on the surface of Ag-doped alumina nanocomposite matched well with LIM ( $R^2=0.9783$ ), while the  $R^2$  value of FIM was 0.9557. Moreover, a Freundlich heterogeneity factor of 0.687 was obtained, indicating excellent sorption of IGC on the surface of the Ag-doped alumina nanocomposite (Hamdaoui and Naffrechoux 2007).

**Thermodynamic**

The effects of temperature and concentration on the removal of IGC by Ag-doped alumina nanocomposite are shown in Fig. 11. The Ag-doped alumina nanocomposite showed an experimental  $q_t$  value of  $462.7 \text{ mg g}^{-1}$  from  $160 \text{ mg L}^{-1}$  at  $50 \text{ }^\circ\text{C}$ . The  $q_t$  value is directly proportional to the temperature in an endothermic process (Darryle et al. 2021). To better understand the sorption of IGC on the surface of the Ag-doped alumina nanocomposite, the thermodynamics were evaluated. The enthalpy ( $\Delta H^\circ$ ) and entropy ( $\Delta S^\circ$ ) were calculated using Eq. (15) and their values were used to determine the Gibbs free energy ( $\Delta G^\circ$ ) using Eq. (16). The results are shown in Table 3.

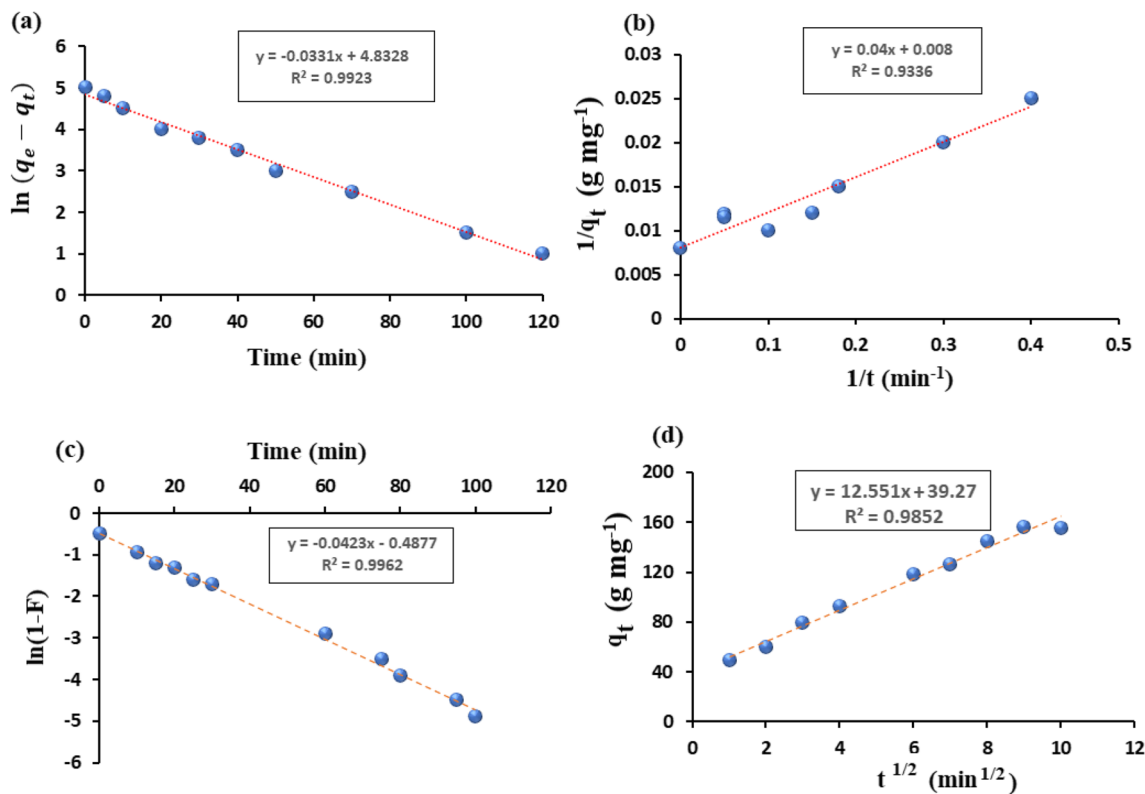


**Fig. 9** Kinetics studies for IGC dye removal including **a** FOM, **b** SOM, **c** LDM, and **d** IM on the surface of Ag-doped alumina nanocomposite

**Fig. 10** The adsorption efficiency of IGC dye on the surface of Ag-doped alumina nanocomposite using **a** LIM and **b** FIM using different concentration (40, 80, 120, 160 mg L<sup>-1</sup>) at 30 °C

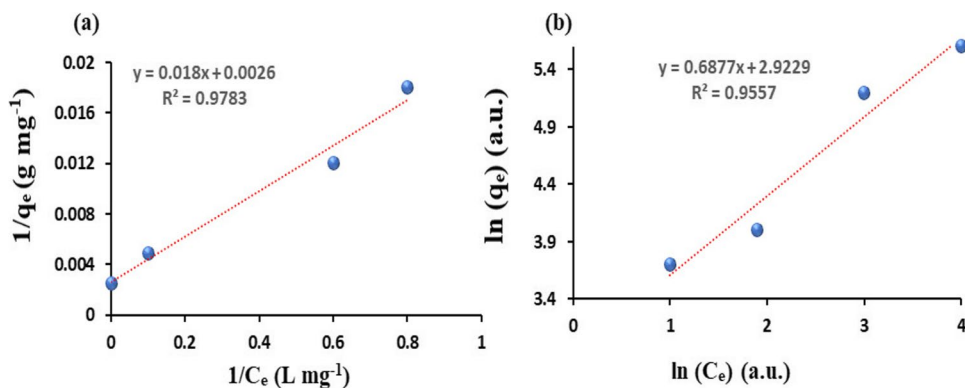


**Table 3** Isotherms and thermodynamic parameters for IGC dye adsorption on the surface of Ag-doped alumina nanocomposite

Adsorption isotherms of IGC on Ag-doped alumina nanocomposite					
Langmuir (LIM)			Freundlich (FIM)		
R <sup>2</sup> (a.u.)	K <sub>L</sub> (L mg <sup>-1</sup> )	q <sub>m</sub> (mg g <sup>-1</sup> )	R <sup>2</sup> (a.u.)	K <sub>f</sub> (L mg <sup>-1</sup> )	n <sup>-1</sup> (a.u.)
0.9783	256.047	0.169	0.9557	56.407	0.687
Thermodynamic parameters					
Fed conc. (mg L <sup>-1</sup> )	ΔH° (kJ mol L <sup>-1</sup> )	ΔS° (kJ mol L <sup>-1</sup> )	ΔG° (kJ mol L <sup>-1</sup> )	ΔG° (kJ mol L <sup>-1</sup> )	ΔG° (kJ mol L <sup>-1</sup> )
40	82.568	0.305	-6.478	-11.789	-16.408
80	57.461	0.314	-7.245	-10.485	-14.396
120	97.982	0.344	-2.817	-8.045	-14.175
160	67.974	0.256	-0.826	-4.283	-7.569

$$\ln K_c = \frac{\Delta H^\circ}{Rt} + \frac{\Delta S^\circ}{R} \quad (15)$$

$$\Delta G^\circ = \Delta H^\circ - T\Delta S^\circ \quad (16)$$

As in the above calculation, the value 0.0081345 kJ mol L<sup>-1</sup> was used as the deal gas constant ( $R$ ). The positive ( $\Delta H^\circ$ ) obtained are in agreement with the previous endothermic results. However, the negative values of ( $\Delta G^\circ$ ) indicate the spontaneity of IGC sorption on the nanocomposite surface (Elamin et al. 2019). Moreover, the results showed that the  $G^\circ$  values were less than 20 kJ mol L<sup>-1</sup>, indicating a physio-sorption process (Elamin et al. 2021). The results showed that the spontaneity of sorption increased with decreasing concentration, indicating the effectiveness of the Ag-doped alumina nanocomposite for the treatment of water, for which a lower concentration was required.

### Application of water sample and Ag-doped alumina nanocomposite regeneration

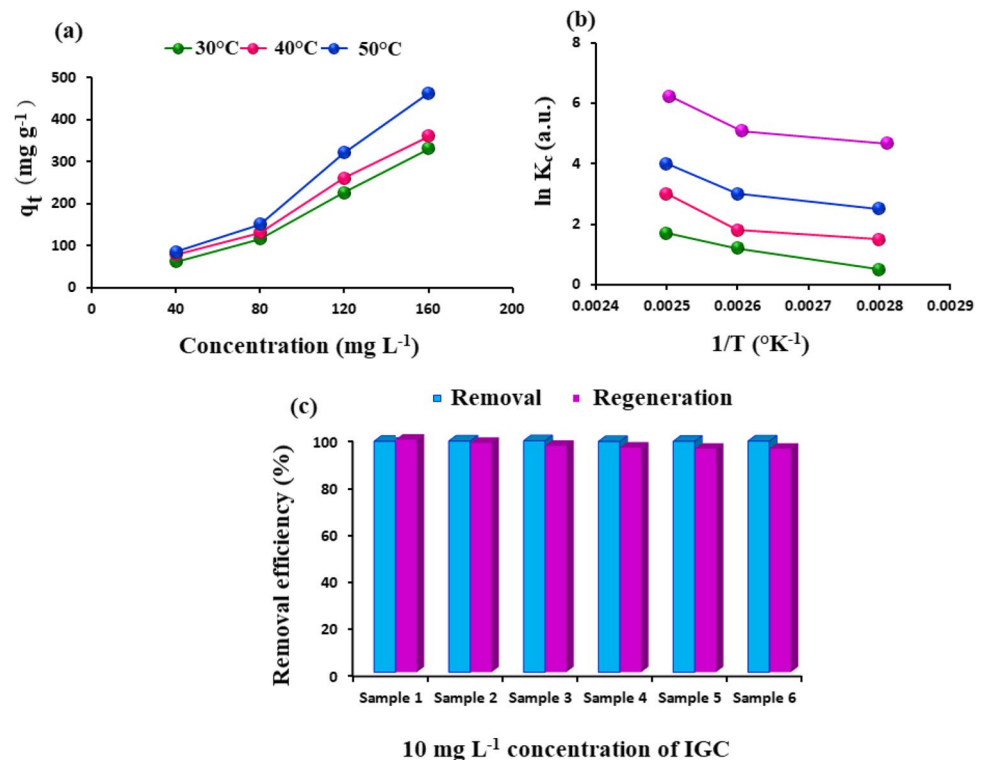
The results showed that the use of nanocomposites to remove IGC from contaminated water samples (Fig. 11 c). The study showed that the nanocomposite effectively treated and completely removed 98.45% of IGC concentration of

10 mg L<sup>-1</sup> in six water samples. In addition, the regeneration of the proposed Ag-doped alumina nanocomposite was tested. The nanocomposite used was filtered and sonicated with 10 mL ethanol for 10 min, followed by 20 mL distilled water, filtered, rinsed with distilled water, and dried at 100 °C for 2 h. The initial removal efficiency was assumed to be 100%, and the subsequent power was approximated. The average efficiency of the Ag-doped alumina nanocomposite was 95.72%, with an RSD value of 3.6%, while the lowest efficiency was 89.32%. This result was consistent with the sorption matching of the LFDM, indicating that the penetration of the contaminant into the internal sorption sites was easy and hindered the recovery.

### Conclusion

A novel Ag-doped alumina nanocomposite with an average size of 100 nm was successfully prepared using coffee husk extract by environmentally friendly biogenic synthesis. The morphological features showed the spherical structure of the Ag-doped alumina nanocomposite with non-uniform distribution of particles. The formed nanocomposite showed the highest surface area (126.58 m<sup>2</sup>g<sup>-1</sup>), average pore diameter (145.95 Å), and average pore volume (0.45 cm<sup>3</sup>g<sup>-1</sup>) in the BET technique. The evaluation of antibacterial capabilities revealed that the

**Fig. 11** **a** The influence of initial fed of IGC concentration on the sorption efficiency of Ag-doped alumina nanocomposite at various temperatures (30, 40, and 50 °C), **b** thermodynamic study of IGC sorption on the surface of Ag-doped alumina nanocomposite using different concentrations at 40, 80, 120, and 160 mg L<sup>-1</sup> at the same temperature degrees, and **c**



Ag-doped alumina nanocomposite possessed significant antibacterial activity with minimum inhibitory concentration of the nanocomposite 12  $\mu\text{g mL}^{-1}$  against *E. coli* and *S. typhi*, two very common water contaminants. The as-synthesized Ag-doped alumina nanocomposite also showed antibacterial activity against both bacterial strains under dark conditions. However, the antibacterial effect of the Ag-doped alumina nanocomposite was comparatively less significant on pathogenic bacteria in the dark. Thus, our results clearly indicate that the pre-synthesized nanocomposite has potential antibacterial properties and could be used to combat waterborne pathogens. Clean water is a vital requirement for life, and our research introduces a novel method for purifying wastewater using Ag-doped alumina nanocomposite. In addition, the nanocomposite has multiple effects as a sorbent to remove IGC from contaminated water. The adsorption order and rate control mechanism for IGC dye adsorption were evaluated on the surface of Ag-doped alumina nanocomposite. The  $R^2$  values for IGC sorption were 0.9923 at a  $K_1$  value of 0.043  $\text{min}^{-1}$  and 0.9336 at a  $K_2$  value of 0.008  $\text{g mg}^{-1} \text{min}^{-1}$  for FOM and SOM, respectively. However, evaluation of the rate control mechanism yielded  $R^2$  values of 0.9962 with an equilibrium constant of 0.034  $\text{mg g}^{-1} \text{min}^{-0.5}$  and 0.9852 with an equilibrium constant of 16.23  $\text{min}^{-1}$  for LDM and IM, respectively. The LFM affected the IGC removal on the surface of the Ag-doped alumina nanocomposite and the IGC adsorption was in accordance with the equilibrium model of LI. However, further research on the other physicochemical properties of the Ag-doped alumina nanocomposite is needed before this material

can be used to purify contaminated water, especially for drinking water purposes.

**Author contribution** All authors contributed to study conception and design. Material preparation, data collection, and analysis were performed by Seham Alterary, Musarat Amina, and Maha El-Tohamy; the draft of first of the manuscript was written by Musarat Amina and Maha F. El-Tohamy. All authors read and approved the final manuscript.

**Funding** This research was funded by Researchers Supporting Project in King Saud University and the code number is (RSP-2023/195).

**Data availability** All data generated or analyzed during this study are included in this published article.

## Declarations

**Ethics approval and consent to participate** Not applicable.

**Consent for publication** Not applicable.

**Competing interests** The authors declare no competing interests.

## References

- Aadil M, Zulfiqar S, Sabeeh H, Warsi MF, Shahid M, Alsafari IA, Shaker I (2020) Enhanced electrochemical energy storage properties of carbon coated  $\text{Co}_3\text{O}_4$  nanoparticles-reduced graphene oxide ternary nano-hybrids. *Ceram Int* 46:17836–17845. <https://doi.org/10.1016/j.ceramint.2020.04.090>



- Aadil M, Mahmood M, Warsi MF, Alsafari IA, Zulfiqar S, Shahid M (2021a) Fabrication of MnO<sub>2</sub> nanowires and their nanohybrid with flat conductive matrix for the treatment of industrial effluents. *FlatChem* 30:100316. <https://doi.org/10.1016/j.flatc.2021.100316>
- Aadil M, Rahman A, Zulfiqar S, Alsafari IA, Shahid M, Shakir I, Agboola PO, Haider S, Warsi MF (2021b) Facile synthesis of binary metal substituted copper oxide as a solar light driven photocatalyst and antibacterial substitute. *Adv Powder Technol* 32:940–950. <https://doi.org/10.1016/j.appt.2021.01.040>
- Aadil M, Hassan W, Somaily HH, Ejaz SR, Abass RR, Jasem H, Hachim SK, Adhab AH, Abood ES, Alsafari IA (2022) Synergistic effect of doping and nanotechnology to fabricate highly efficient photocatalyst for environmental remediation. *J Alloys Compd* 920:165876. <https://doi.org/10.1016/j.jallcom.2022.165876>
- Aamir M, Bibi I, Ata S, Jilani K, Majid F, Kamal S, Alwadi N, Raza MA, Bashir M, Iqbal S, Aadil M (2021) Ferroelectric, dielectric, magnetic, structural and photocatalytic properties of Co and Fe doped LaCrO<sub>3</sub> perovskite synthesized via microemulsion route. *Ceram Int* 47:16696–16707. <https://doi.org/10.1016/j.ceramint.2021.02.240>
- Adeleye AS, Conway JR, Garner K, Huang Y, Su Y, Keller AA (2016) Engineered nanomaterials for water treatment and remediation: costs, benefits, and applicability. *Chem Eng J* 286:640–662. <https://doi.org/10.1016/j.cej.2015.10.105640-662>
- Al-Juboori RA, Al-Shaeli M, Aani SA, Johnson D, Hilal N (2022) Membrane technologies for nitrogen recovery from waste streams: scientometrics and technical analysis. *Membranes* 13:15. <https://doi.org/10.1016/j.seppur.2022.120529>
- Alovisi M, Pasqualini D, Mandras N, Roana J, Costamagna P, Comba A, Cavalli R, Luginani A, Iandolo A, Cavallo L, Scotti N (2022) Confocal laser scanner evaluation of bactericidal effect of chitosan nanodroplets loaded with benzalkonium chloride. *J Clin Med* 11:1650. <https://doi.org/10.3390/jcm11061650>
- An B (2020) Cu (II) and As (V) adsorption kinetic characteristic of the multifunctional amino groups in chitosan. *Processes* 8:1194. <https://doi.org/10.3390/pr8091194>
- Angulo-Bejarano PI, Puente-Rivera J, Cruz-Ortega R (2021) Metal and metalloid toxicity in plants: an overview on molecular aspects. *Plants* 10:635. <https://doi.org/10.3390/plants10040635>
- Aparna Z, Michael M, Pabi SK, Ghosh S (2019) Thermal conductivity of aqueous Al<sub>2</sub>O<sub>3</sub>/Ag hybrid nanofluid at different temperatures and volume concentrations: an experimental investigation and development of new correlation function. *Powder Technol* 343:714–722. <https://doi.org/10.1016/j.powtec.2018.11.096>
- Asadpour S, Raeisi Vanani A, Kooravand M, Asfaram A (2022) A review on zinc oxide/poly (vinyl alcohol) nanocomposites: synthesis, characterization and applications. *J Clean Prod* 362:132297. <https://doi.org/10.1016/j.jclepro.2022.132297>
- Astuti RD, Mallongi A, Amiruddin R, Hatta M, Rauf AU (2023) Hexavalent chromium contamination in groundwater and its implication to human health: a Monte Carlo model approach in Indonesia. *Sustain Water Resour Manag* 9:1–3. <https://doi.org/10.1002/9781119709732.ch8>
- Atrak K, Ramazani A, Taghavi Fardood S (2018) Green synthesis of amorphous and gamma aluminum oxide nanoparticles by tragacanth gel and comparison of their photocatalytic activity for the degradation of organic dyes. *J Mater Sci: Mater Electron* 29:8347–8353. <https://doi.org/10.1007/s10854-018-8845-2>
- Baghayeri M, Veisi H, Farhadi S, Beitollahi H, Maleki B (2018) Ag nanoparticles decorated Fe<sub>3</sub>O<sub>4</sub>/chitosan nanocomposite: synthesis, characterization and application toward electrochemical sensing of hydrogen peroxide. *J Iran Chem Soc* 15:1015–1022. <https://doi.org/10.1007/s13738-018-1298-y>
- Balabel A, Alwetaishi M (2021) Toward sustainable healthcare facilities: an initiative for Development of Mostadam-HCF” rating system in Saudi Arabia. *Sustainability* 13:6742. <https://doi.org/10.3390/su13126742>
- Bibi F, Iqbal S, Sabeeh H, Saleem T, Ahmad B, Nadeem M, Shakir I, Aadil M, Kalsoom A (2021) Evaluation of structural, dielectric, magnetic and photocatalytic properties of Nd and Cu co-doped barium hexaferrite. *Ceram Int* 47:30911–30921. <https://doi.org/10.1016/j.ceramint.2021.07.274>
- Calovi M, Furlan B, Coroneo V, Massidda O, Rossi S (2021) Facile route to effective antimicrobial aluminum oxide layer realized by co-deposition with silver nitrate. *Coatings* 12:28. <https://doi.org/10.3390/coatings12010028>
- Cangussu LB, Melo JC, Franca AS, Oliveira LS (2021) Chemical characterization of coffee husks, a by-product of coffee arabica production. *Foods* 10:3125. <https://doi.org/10.3390/foods10123125>
- Chakraborty V, Das P, Roy PK (2021) Synthesis and application of various metal oxide–biomaterial–coated carbonaceous nanomaterials derived from waste biomass for removal of Cr<sup>6+</sup> present in solution. *Biomass Convers Biorefin* 3:1–4. <https://doi.org/10.1007/s13399-020-01224-9>
- Cruz G, Braz CE, Ferreira SL, dos Santos AM, Crnkovic PM (2013) Physicochemical properties of brazilian biomasses: potential applications as renewable energy source. In 22nd International Congress of Mechanical Engineering (COBEM 2013), Ribeirão Preto, Brazil, 3–7. <http://www.academicjournals.org/AJB>
- Dar UA, Salunke-Gawali S, Shinde D, Bh S, Satpute S (2021) Thermal and spectral studies of transition metal complexes of 2-bromo-3-hydroxynaphthalene-1, 4-dione: evaluation of antibacterial activity against six bacterial strains. *Eng Sci* 15:105–115. <https://doi.org/10.30919/es8d492>
- Darryle CM, Acayanka E, Takam B, Line LN, Kamgang GY, Laminsi S, Sellaoui L, Bonilla-Petriciolet A (2021) Influence of plasma-based surface functionalization of palm fibers on the adsorption of diclofenac from water: experiments, thermodynamics and removal mechanism. *J Water Process Eng* 43:102254. <https://doi.org/10.1016/j.jwpe.2021.102254>
- Dou S, Ke XX, Shao ZD, Zhong LB, Zhao QB, Zheng YM (2022) Fish scale-based biochar with defined pore size and ultrahigh specific surface area for highly efficient adsorption of ciprofloxacin. *Chemosphere* 287:131962. <https://doi.org/10.1016/j.chemosphere.2021.131962>
- Ekrikaya S, Yilmaz E, Celik C, Demirbuga S, Ildiz N, Demirbas A, Ocsay I (2021) Investigation of ellagic acid rich-berry extracts directed silver nanoparticles synthesis and their antimicrobial properties with potential mechanisms towards *Enterococcus faecalis* and *Candida albicans*. *J Biotechnol* 341:155–162. <https://doi.org/10.1016/j.jbiotec.2021.09.020>
- Elamin MR, Abdulkhair BY, Elzupir AO (2019) Insight to aspirin sorption behavior on carbon nanotubes from aqueous solution: thermodynamics, kinetics, influence of functionalization and solution parameters. *Sci Rep* 9:12795. <https://doi.org/10.1038/s41598-019-49331-6>
- Elamin MR, Abdulkhair BY, Algethami FK, Khezami L (2021) Linear and nonlinear investigations for the adsorption of paracetamol and metformin from water on acid-treated clay. *Sci Rep* 11:1–3. <https://doi.org/10.1038/s41598-021-93040-y>
- Elamin MR, Abdulkhair BY, Elzupir AO (2023) Removal of ciprofloxacin and indigo carmine from water by carbon nanotubes fabricated from a low-cost precursor: solution parameters and recyclability. *Ain Shams Eng J* 14:101844. <https://doi.org/10.1016/j.asej.2022.101844>
- Ezealigo US, Ezealigo BN, Aisida SO, Ezema FI (2021) Iron oxide nanoparticles in biological systems: antibacterial and toxicology perspective. *JCIS Open* 4:100027. <https://doi.org/10.1016/j.jciso.2021.100027>
- Feret FR, Roy D, Boulanger C (2000) Determination of alpha and beta alumina in ceramic alumina by X-ray diffraction. *Spectrochim*

- Acta, Part B 55:1051–1061. [https://doi.org/10.1016/S0584-8547\(00\)00225-1](https://doi.org/10.1016/S0584-8547(00)00225-1)
- Garcia CR, Malik MH, Biswas S, Tam VH, Rumbaugh KP, Li W, Liu X (2022) Nanoemulsion delivery systems for enhanced efficacy of antimicrobials and essential oils. *Biomater Sci* 10:633–653. <https://doi.org/10.1039/D1BM01537K>
- Godoy-Gallardo M, Eckhard U, Delgado LM, de Roo Puente YJ, Hoyos-Nogués M, Gil FJ, Perez RA (2021) Antibacterial approaches in tissue engineering using metal ions and nanoparticles: from mechanisms to applications. *Bioact Mater* 6:4470–4490. <https://doi.org/10.1016/j.bioactmat.2021.04.033>
- Hamdaoui O, Naffrechoux E (2007) Modeling of adsorption isotherms of phenol and chlorophenols onto granular activated carbon: Part I. Two-parameter models and equations allowing determination of thermodynamic parameters. *J Hazard Mater* 147:381–394. <https://doi.org/10.1016/j.jhazmat.2007.01.021>
- Hameed BH, El-Khaiary MI (2008) green adsorption by rattan sawdust: isotherm, kinetic and mechanism modeling. *J Hazard Mater* 159:574–579. <https://doi.org/10.1016/j.jhazmat.2008.02.054>
- Hassanpour P, Panahi Y, Ebrahimi-Kalan A, Akbarzadeh A, Davaran S, Nasibova AN, Khalilov R, Kavetskyy T (2018) Biomedical applications of aluminium oxide nanoparticles. *Micro Nano Lett* 13:1227–1231. <https://doi.org/10.1049/mnl.2018.5070>
- Hiawi FA, Ali IH (2022) Study the adsorption behavior of food colorant dye indigo carmine and loratadine drug in solution. *Chem Methodol* 6:720–730
- Holzwarth U, Gibson N (2011) The Scherrer equation versus the Debye-Scherrer equation. *Nat Nanotechnol* 6:534. <https://doi.org/10.1038/nnano.2011.145>
- Jabbar KQ, Barzinjy AA, Hamad SM (2022) Iron oxide nanoparticles: preparation methods, functions, adsorption and coagulation/flocculation in wastewater treatment. *Environ Nanotechnol, Monit Manag* 17:100661. <https://doi.org/10.1016/j.enmm.2022.100661>
- Jagminas A, Žalneravičius R, Rėza A, Paškevičius A, Selskienė A (2015) Design, optical and antimicrobial properties of extremely thin alumina films colored with silver nanospecies. *Dalton Trans* 44:4512–4519. <https://doi.org/10.1039/C4DT03644A>
- Janissen B, Huynh T (2018) Chemical composition and value-adding applications of coffee industry by-products: a review. *Resour Conserv Recycl* 128:110–117. <https://doi.org/10.1016/j.rescon.2017.10.001>
- Jimenez-Reyes M, Almazan-Sanchez PT, Solache-Rios M (2021) Radioactive waste treatments by using zeolites. A short review. *J Environ Radioact* 233:106610. <https://doi.org/10.1016/j.jenvrad.2021.106610>
- Karthigadevi G, Manikandan S, Karmegam N, Subbaiya R, Chozhavanthhan S, Ravindran B, Chang SW, Awasthi MK (2021) Chemical-nanotreatment methods for the removal of persistent organic pollutants and xenobiotics in water—a review. *Bioresour Technol* 324:124678. <https://doi.org/10.1016/j.biortech.2021.124678>
- Khatami M, Irvani S (2021) Green and eco-friendly synthesis of nanophotocatalysts: an overview. *Comments Inorg Chem* 41:133–187. <https://doi.org/10.1080/02603594.2021.1895127>
- Kiradzhyska D, Milcheva N, Batsalova T, Dzhambazov B, Zahariev N, Mancheva R (2022) Silver-doped anodic alumina with antimicrobial properties-synthesis and characterization. *Metals* 12:474. <https://doi.org/10.3390/met12030474>
- Kiseleva MA, Sokovnin SY, Balezin ME (2019) Synthesis and characterization of Al<sub>2</sub>O<sub>3</sub> +Ag composite nanopowders. In *AIP Conf Proc* 2174:020031. <https://doi.org/10.1063/1.5134182>
- Koh KY, Yang Y, Chen JP (2022) Critical review on lanthanum-based materials used for water purification through adsorption of inorganic contaminants. *Crit Rev Environ Sci Technol* 52:1773–1823. <https://doi.org/10.1080/10643389.2020.1864958>
- Kousar T, Aadil M, Zulfiqar S, Warsi MF, Ejaz SR, Elnaggar AY, Fallatah AM, El-Bahy SM, Mahmood F (2022) Wet-chemical synthesis of nanostructured Ce-doped mixed metal ferrites for the effective removal of azo dyes from industrial discharges. *Ceram Int* 48(8):11858–11868. <https://doi.org/10.1016/j.ceramint.2022.01.057>
- Kristanti RA, Hadibarata T, Syafrudin M, Yılmaz M, Abdullah S (2022) Microbiological contaminants in drinking water: current status and challenges. *Water Air Soil Pollut* 233:1–7. <https://doi.org/10.1007/s11270-022-05698-3>
- Kumar P, Srivastava S, Banerjee A, Banerjee S (2022) Prevalence and predictors of water-borne diseases among elderly people in India: evidence from Longitudinal Ageing Study in India, 2017–18. *BMC Public Health* 22:1–1. <https://doi.org/10.1186/s12889-022-13376-6>
- Lanje AS, Sharma SJ, Pode RB (2010) Synthesis of silver nanoparticles: a safer alternative to conventional antimicrobial and antibacterial agents. *J Chem Pharm Res* 2:478–483
- Lewoyehu M (2021) Comprehensive review on synthesis and application of activated carbon from agricultural residues for the remediation of venomous pollutants in wastewater. *J Anal Appl Pyrolysis* 159:105279. <https://doi.org/10.1016/j.jaap.2021.105279>
- Lotfy HR, Roubik H (2021) Water purification using activated carbon prepared from agriculture waste—overview of a recent development. *Biomass Convers Biorefin* 31:1–4. <https://doi.org/10.1007/s13399-021-01618-3>
- Luo J, Ser W, Liu A, Yap PH, Liedberg B, Rayatpisheh S (2022) Low complexity and accurate machine learning model for waterborne pathogen classification using only three handcrafted features from optofluidic images. *Biomed Signal Process Control* 77:103821. <https://doi.org/10.1016/j.bspc.2022.103821>
- Maleki B, Baghayeri M, Vahdat SM, Mohammadzadeh A, Akhoondi S (2015) Ag@TiO<sub>2</sub> nanocomposite; synthesis, characterization and its application as a novel and recyclable catalyst for the one-pot synthesis of benzoxazole derivatives in aqueous media. *RSC Adv* 5:46545–46551. <https://doi.org/10.1039/C5RA06618B>
- Manikandan V, Jayanthi P, Priyadharsan A, Vijayapathap E, Anbarasan PM, Velmurugan P (2019) Green synthesis of pH-responsive Al<sub>2</sub>O<sub>3</sub> nanoparticles: application to rapid removal of nitrate ions with enhanced antibacterial activity. *J Photochem Photobiol, A* 371:205–215. <https://doi.org/10.1016/j.jphotochem.2018.11.009>
- Maximov M, Maximov OC, Craciun L, Ficai D, Ficai A, Andronescu E (2021) Bioactive glass—an extensive study of the preparation and coating methods. *Coatings* 11:1386. <https://doi.org/10.3390/coatings11111386>
- Mokhena TC, Luyt AS (2017) Electrospun alginate nanofibres impregnated with silver nanoparticles: preparation, morphology and antibacterial properties. *Carbohydr Polym* 165:304–312. <https://doi.org/10.1016/j.carbpol.2017.02.068>
- Nasrollahzadeh M, Issaabadi Z, Sajadi SM (2019) Green synthesis of the Ag/Al<sub>2</sub>O<sub>3</sub> nanoparticles using Bryonia alba leaf extract and their catalytic application for the degradation of organic pollutants. *J Mater Sci: Mater Electron* 30:3847–3859. <https://doi.org/10.1007/s10854-019-00668-8>
- Prabhakar R, Samadder SR (2018) Low cost and easy synthesis of aluminium oxide nanoparticles for arsenite removal from groundwater: a complete batch study. *J Mol Liq* 250:192–201. <https://doi.org/10.1016/j.molliq.2017.11.173>
- Puchalski M, Dąbrowski P, Olejniczak W, Krukowski P, Kowalczyk P, Polański K (2007) The study of silver nanoparticles by scanning electron microscopy, energy dispersive X-ray analysis and scanning tunnelling microscopy. *Mater Sci-Pol* 25:473–478
- Rahman A, Aadil M, Zulfiqar S, Alsafari IA, Shahid M, Agboola PO, Warsi MF, Abdel-Halim ME (2021) Fabrication of binary metal substituted CdO with superior aptitude for dye degradation and antibacterial activity. *Ceram Int* 47:8082–8093. <https://doi.org/10.1016/j.ceramint.2020.11.163>

- Rajoriya P, Barcelos M, Ferreira D, Misra P, Molina G, Pelissari FM, Shukla PK, Ramteke PW (2021) Green silver nanoparticles: recent trends and technological developments. *J Polym Environ* 29:2711–2737. <https://doi.org/10.1007/s10924-021-02071-z>
- Rashid R, Shafiq I, Akhter P, Iqbal MJ, Hussain M (2021) A state-of-the-art review on wastewater treatment techniques: the effectiveness of adsorption method. *Environ Sci Pollut Res* 28:9050–9066. <https://doi.org/10.1007/s11356-021-12395-x>
- Ravindhranath K, Ramamoorthy M (2017) Nano aluminum oxides as adsorbents in water remediation methods: a review. *Rasayan J Chem* 10:716–722. <http://www.rasayanjournal.co.in/>
- Raza A, Altaf S, Ali S, Ikram M, Li G (2022) Recent advances in carbonaceous sustainable nanomaterials for wastewater treatments. *Sustain Mater Technol* 17:e00406. <https://doi.org/10.1016/j.susmat.2022.e00406>
- Reis N, Franca AS, Oliveira LS (2013) Discrimination between roasted coffee, roasted corn and coffee husks by Diffuse Reflectance Infrared Fourier Transform Spectroscopy. *LWT Food Sci Technol* 50:715–722
- Ribeiro EF, Luzia DMM, Jorge N (2019) Antioxidant compounds extraction from coffee husks: the influence of solvent type and ultrasound exposure time. *Acta Scientiarum Technol* 41:e36451–e36451. <http://orcid.org/0000-0002-3755-9735>
- Roque-Ruiz JH, Castillo-Ramírez D, de Jesús R-B, Espinosa-Cristóbal LF, Reyes-López SY (2018) Preparation of silver-doped alumina spherical beads with antimicrobial properties. *J Nanomater* 2018:7127843. <https://doi.org/10.1155/2018/7127843>
- Roy D (2021) Aluminum-doped nano-zinc oxide an act as good carrier for biomedicine. In *Advances in medical physics and healthcare engineering*. Springer, Singapore, 2020:145–152. [https://doi.org/10.1007/978-981-33-6915-3\\_15](https://doi.org/10.1007/978-981-33-6915-3_15)
- Sajjadifar S (2017) Silica Boron sulfonic acid as a new and efficient catalyst for the green synthesis of quinoxaline derivatives at room temperature. *Chem Methodol* 1:1–14. <https://doi.org/10.22631/chemm.2017.88920.1000>
- Shameli K, Aid SR, Jonny NF, Asako Y (2021) Green synthesis of gold nanoparticles based on plant extract for anofluid-based hybrid photovoltaic system application. *J Res Nanosci Nanotechnol* 4:19–34. <https://doi.org/10.37934/jrnn.4.1.1934>
- Sharma G, AlGarni TS, Kumar PS, Bhogal S, Kumar A, Sharma S, Naushad M, ALOthman ZA, Stadler FJ (2021) Utilization of Ag<sub>2</sub>O–Al<sub>2</sub>O<sub>3</sub>–ZrO<sub>2</sub> decorated onto rGO as adsorbent for the removal of Congo red from aqueous solution. *Environ Res* 197:111179. <https://doi.org/10.1016/j.envres.2021.111179>
- Shokri A, Fard MS (2022) A critical review in electrocoagulation technology applied for oil removal in industrial wastewater. *Chemosphere* 288:132355. <https://doi.org/10.1016/j.chemosphere.2021.132355>
- Singh R, Singh M, Kumari N, Maharana S, Maharana P (2021b) A comprehensive review of polymeric wastewater purification membranes. *J Compos Sci* 5:162. <https://doi.org/10.3390/jcs5060162>
- Singh J, Gupta P, Das A (2021a) Dyes from textile industry wastewater as emerging contaminants in agricultural fields. *Sustainable Agriculture Reviews*. Springer, Cham, 50:109–129. [https://doi.org/10.1007/978-3-030-63249-6\\_5](https://doi.org/10.1007/978-3-030-63249-6_5)
- Song X, Zhu W, Pei Y, Ai Z, Chen J (2013) Effects of wheat bran with different colors on the qualities of dry noodles. *J Cereal Sci* 58:400–407. <https://doi.org/10.1016/j.jcs.2013.08.005>
- Sumra AA, Aadil M, Ejaz SR, Anjum S, Saleem T, Zain M, Alsafari IA (2022) Biological synthesis of nanostructured ZnO as a solar-light driven photocatalyst and antimicrobial agent. *Ceram Int* 48:14652–14661. <https://doi.org/10.1016/j.ceramint.2022.01.359>
- Tizian K, Jonathan IK, Vera G, Tabata RR, Steffen S, Dirk WL (2020) A review of coffee by-products including leaf, flower, cherry, husk, silver skin, spent grounds as novel foods within the European Union. *Foods* 9:665. <https://doi.org/10.3390/foods9050665>
- Touqeer M, Baig MM, Aadil M, Agboola PO, Shakir I, Aboud MF, Warsi MF (2020) New Co-MnO based nanocrystallite for photocatalysis studies driven by visible light. *J Taibah Univ Sci* 14:1580–1589. <https://doi.org/10.1080/16583655.2020.1846966>
- Tungmunthum D, Thongboonyou A, Pholboon A, Yangsabai A (2018) Flavonoids and other phenolic compounds from medicinal plants for pharmaceutical and medical aspects: an overview. *Medicines* 5:93. <https://doi.org/10.3390/medicines5030093>
- Wang X, Wang S, Zhang Y (2016) Advance of the application of nano-controlled release system in ophthalmic drug delivery. *Drug Deliv* 23:2897–2901. <https://doi.org/10.3109/10717544.2015.1116025>
- Wang L, Shi C, Pan L, Zhang X, Zou JJ (2020) Rational design, synthesis, adsorption principles and applications of metal oxide adsorbents: a review. *Nanoscale* 12:4790–4815. <https://doi.org/10.1039/C9NR09274A>
- Xie J, Lin Y, Li C, Wu D, Kong H (2015) Removal and recovery of phosphate from water by activated aluminum oxide and lanthanum oxide. *Powder Technol* 269:351–357. <https://doi.org/10.1016/j.powtec.2014.09.024>
- Yang X, Li Q, Wang H, Huang J, Lin L, Wang W, Sun D, Su Y, Opiyo JB, Hong L, Wang Y (2010) Green synthesis of palladium nanoparticles using broth of *Cinnamomum camphora* leaf. *J Nanopart Res* 12:1589–1598. <https://doi.org/10.1007/s11051-009-9675-1>
- Yang D, Huang S, Ruan M, Li S, Yang J, Wu Y, Guo W, Zhang L (2018) Mussel inspired modification for aluminum oxide/silicone elastomer composites with largely improved thermal conductivity and low dielectric constant. *Ind Eng Chem Res* 57:3255–3262. <https://doi.org/10.1021/acs.iecr.7b04970>
- Zhang L, Meng G, Fan G, Chen K, Wu Y, Liu J (2021) High flux photocatalytic self-cleaning nanosheet C3N4 membrane supported by cellulose nanofibers for dye wastewater purification. *Nano Res* 14:2568–2573. <https://doi.org/10.1007/s12274-020-3256-0>
- Zhao ZY, Li PJ, Xie RS, Cao XY, Su DL, Shan Y (2022) Biosynthesis of silver nanoparticle composites based on hesperidin and pectin and their synergistic antibacterial mechanism. *Int J Biol Macromol* 214:220–229. <https://doi.org/10.1016/j.ijbiomac.2022.06.048>
- Zhou J, Zhang J, Guo X, Mao J, Zhang S (2012) Ag/Al<sub>2</sub>O<sub>3</sub> for glycerol hydrogenolysis to 1, 2-propanediol: activity, selectivity and deactivation. *Green Chem* 14:156–163. <https://doi.org/10.1039/C1GC15918F>
- Zuorro A, Iannone A, Miglietta S, Lavecchia R (2022) Green synthesis of silver nanoparticles using spent coffee ground extracts: process modelling and optimization. *Nanomaterials* 12:2597. <https://doi.org/10.3390/nano12152597>

**Publisher's note** Springer Nature remains neutral with regard to jurisdictional claims in published maps and institutional affiliations.

Springer Nature or its licensor (e.g. a society or other partner) holds exclusive rights to this article under a publishing agreement with the author(s) or other rightsholder(s); author self-archiving of the accepted manuscript version of this article is solely governed by the terms of such publishing agreement and applicable law.